

Fast hardware-aware matrix-free computations of higher-order finite-element discretized matrix multi-vector products

Nikhil Kodali^{a,1}, Gourab Panigrahi^{a,1}, Debashis Panda^{a,2}, Phani Motamarri^a

^aDepartment of Computational and Data Sciences, Indian Institute of Science, CV Raman Road, Bengaluru, 560012, Karnataka, India

Abstract

Recent hardware-aware algorithms for higher-order finite-element (FE) discretized matrix-vector multiplications suggest that on-the-fly matrix-vector products can reduce arithmetic complexity and improve data access efficiency. These matrix-free approaches leverage the tensor-structured nature of the FE polynomial basis to evaluate the underlying integrals without explicitly constructing the global sparse matrix. Furthermore, iterative solvers for large-scale eigenvalue problems or linear systems of equations with multiple RHS vectors arising from FE discretizations necessitate efficient matrix-multivector products involving multiple vectors. However, the current state-of-the-art implementations of such matrix-free algorithms are well-suited for the action of FE-discretized matrices on a single vector and are not directly applicable to matrix-multivector products with many vectors. In this work, we propose a computationally efficient and scalable matrix-free implementation procedure for computing FE-discretized matrix-multivector products on both multi-node CPU and GPU architectures. Our implementation achieves 1.6x – 3.1x improvement on multi-node GPU architectures and 1.6x – 4.4x on multi-node CPU architectures for matrix-multivector products compared to the closest baseline implementation when using 1024 vectors and FE interpolating polynomial orders in the range 6 to 8.

Keywords: Matrix-free, Finite Element Method, sum factorization, parallelization

1. Introduction

Finite-element (FE) based numerical approaches are routinely employed to solve partial differential equations arising in various areas of science and engineering. The finite-element (FE) solution of a partial differential equation usually involves constructing a discretized operator, often a sparse matrix, due to the compact support of the FE basis functions. In this framework, the PDE reduces to a sparse system of linear equations (in case of boundary-value problems) or sparse matrix eigenvalue problems (in case of eigenproblems). These sparse matrix problems are traditionally solved using iterative solvers, which require computing the action of the sparse matrix on trial FE discretized fields for the solution of a linear system of equations or eigenvalue problems (usually utilizing iterative solvers). Evaluation of the product of the sparse matrix and the vector (FE discretized field) is usually the computationally demanding step. It is traditionally computed using sparse-matrix vector multiplication modules. However, previous works such as [1] note that the evaluation of such sparse matrix-vector products can be done more efficiently on multithreaded architectures using cell-level dense matrix-vector multiplications followed by the assembly of cell-level product vectors. Motamarri et al. [2], Das et al. [3] have recently employed this strategy on multi-node

CPU and GPU architectures for evaluating the cell-level dense matrix-multivector products involving a large number of vectors (>300). They demonstrate good throughput performance for the solution of FE-discretized large-scale nonlinear eigenvalue problems arising in the quantum modeling of materials using density functional theory. However, recent hardware-aware algorithms for evaluating such matrix-vector multiplications suggest that on-the-fly matrix-vector products without storing the cell-level dense matrices reduce both arithmetic complexity and memory footprint[4–7]. These algorithms, referred to as matrix-free approaches, exploit the tensor-structured nature of the finite-element basis functions and recast the 3D integrals involved in the matrix-vector products as a sequence of tensor contractions.

The open-source implementations of the above matrix-free methods currently available to the community [8–11] are neither optimal nor directly applicable for the action of a FE discretized operator on a large number of FE discretized fields. One often encounters such situations while solving FE-discretized eigenvalue problems [12, 13] using iterative orthogonal projection approaches or solving linear systems of equations arising from FE discretizations with multiple RHS vectors. These problems arise in real-space quantum modeling of materials[3, 14, 15] or in scientific machine learning to train ML models with the solutions of FE discretized partial differential equations with multiple forcing vectors[16]. Although some preliminary work [17, 18] exists in this regard, no widely available implementation procedures exist for performing generic FE discretized matrix-multivector efficiently under the matrix-free paradigm.

This work proposes an efficient hardware-aware implemen-

Email address: phanim@iisc.ac.in (Phani Motamarri)

¹Nikhil Kodali and Gourab Panigrahi contributed equally to this work.

²Currently at Department of Chemical Engineering in Imperial College London, U.K.

tation procedure for the matrix-free algorithm to compute such FE-discretized matrix-multivector products on multi-node CPU-only and multi-node GPU architectures. As traditionally done in finite-element literature, we partition the physical domain into non-overlapping subdomains, each assigned to an MPI task, and use the MPI paradigm to communicate the boundary data across multiple nodes. We will briefly discuss the theory and implementation aspects of this strategy in Sections 2 and 3.1.5 respectively. On CPU architectures, we utilize the SIMD vectorization capabilities of modern CPU architectures along with optimal implementation strategies which exploit the symmetry of the problem (such as the *even-odd* decomposition[19, 20]) to minimize the computation time and use non-blocking MPI communications to overlap computation and communication, allowing for higher scaling efficiencies. On GPU-based architectures, the proposed matrix-free implementation utilizes the concept of kernel fusion to minimize data access. It also efficiently utilizes the GPU shared memory and registers to pipeline data access and computation.

In Section 2, we provide a concise account of the theoretical foundations underpinning the problem commonly encountered in quantum material modeling, utilizing a finite-element-based discretization technique. Subsequently, we delve deeper into the mathematical underpinnings of the cell-matrix and matrix-free methods as applied to multi-vectors, specifically focusing on the utilization of adaptively refined hexahedral meshes. Furthermore, we present an in-depth examination of the various techniques for evaluating matrix-multivector products within these frameworks, such as subdomain partitioning, the imposition of constraints to ensure continuity, and the extraction of FE-cell level representations, among others.

In Section 3, we delve into the implementation strategies employed to evaluate matrix-multivector products in the matrix-free paradigm. A key consideration in this context is the adaptation of the implementation to the specific characteristics of the underlying hardware architecture. With this in mind, we propose a batched implementation strategy in which we concurrently process a limited subset of vectors, known as a batch. The dimension of this batch is chosen based on the properties of the underlying hardware architecture. We also propose a batched layout for storing the multi-vectors, dramatically improving the data locality for the batched implementation strategy. Furthermore, we provide a summary of the methods used for the imposition of constraints, the extraction of FE-cell level representations, and other relevant operations. We subsequently furnish a comprehensive description of the strategy employed for the implementation of the tensor contractions on both CPU-only and GPU-based architectures in Section 3.1.4.

In Section 4, we benchmark the performance of our implementation using a representative FE-discretized matrix, specifically the Helmholtz problem as our model problem. We use a cell-matrix implementation and the existing matrix-free implementation from the `deal.II` library as our benchmark implementations. Our implementation outperforms the `deal.II` matrix-free implementation on a single GPU ($\sim 360k$ DoFs/GPU) with a speedup of 18.3x for the single vector case with polynomial order 7. As such, we do not consider the `deal.II`

method as a benchmark for multi-vectors on GPU architectures. Our results indicate the superior performance of our proposed implementation, demonstrating computational gains of up to 3.1x on 1 GPU ($\sim 390k$ DoFs/GPU), 1.6x on 8 GPUs ($\sim 49k$ DoFs/GPU), and 4.4x on 768 CPU cores (~ 920 DoFs/core) for matrix-multivector products (1024 vectors) compared to the closest benchmark implementation for polynomial order 8. Additionally, we present the strong scaling studies of our proposed implementation on both multi-node CPU and GPU architectures.

2. Methodology

2.1. Mathematical background

Consider a partial differential equation (PDE) defined on a bounded domain $\Omega \subset \mathbb{R}^3$ involving the differential operator $\mathcal{F} = -\mu \nabla^2 + \kappa(\mathbf{x})$ with $\mu \in \mathbb{R}$ and $\kappa(\mathbf{x}) : \Omega \rightarrow \mathbb{R}$ denoting the system parameters. Note that the operator \mathcal{F} reduces to the Laplacian operator if $\mu = 1$, $\kappa(\mathbf{x}) = 0 \quad \forall \mathbf{x} \in \Omega$ and to the Helmholtz operator if $\mu = 1$, $\kappa(\mathbf{x}) = k^2 \quad \forall \mathbf{x} \in \Omega$ where $k \in \mathbb{R}$ is a constant.

In order to elucidate our matrix-free multi-vector implementation, we introduce the following boundary value problem of finding $u^\beta(\mathbf{x}) \in \mathcal{V}$ with $\beta = 1, 2, \dots, n_v$ such that

$$\begin{aligned} \mathcal{F} u^\beta(\mathbf{x}) &= -\mu \nabla^2 u^\beta(\mathbf{x}) + \kappa(\mathbf{x}) u^\beta(\mathbf{x}) = \begin{cases} f^\beta(\mathbf{x}) \\ \lambda^\beta u^\beta(\mathbf{x}) \end{cases} \quad \forall \mathbf{x} \in \Omega \\ u^\beta(\mathbf{x}) &= u_D(\mathbf{x}) \quad \forall \mathbf{x} \in \partial\Omega_D \end{aligned} \quad (1)$$

where \mathcal{V} denotes a suitable function space in which the solution of the boundary value problem (Eq. (1)) lies, and $u_D(\mathbf{x})$ in the above equation corresponds to the Dirichlet boundary condition. If the choice of RHS is $f^\beta(\mathbf{x}) : \Omega \rightarrow \mathbb{R}$, a set of forcing functions for $\beta = 1, 2, \dots, n_v$, the above problem represents a set of linear PDEs. If the choice of RHS is $\lambda^\beta u^\beta(\mathbf{x})$, then the Eq. (1) represents an eigenvalue problem corresponding to the operator \mathcal{F} with λ_β as eigenvalues and $u^\beta(\mathbf{x})$ as eigenfunctions. Eigenvalue problems of this nature with large n_v are very similar to those arising in the area of quantum-modeling of materials using Kohn-Sham density functional theory (DFT) [3, 21].

We now consider the discretization of the boundary value problem (Eq. (1)) using a finite-element (FE) basis set, a strictly local piecewise polynomial set comprising of C^0 continuous Lagrange polynomials generated using Gauss Lobatto Legendre (GLL) nodal points [22]. To this end, consider the finite-dimensional space $\mathbb{V}_m^h \subset \mathcal{V}$ with a 3D tensor-structured FE basis $N_J^h(\mathbf{x}) : 1 \leq J \leq m$ constructed from the strictly local 1D Lagrange interpolating polynomials of order $n_p - 1$ generated using the nodes of the FE triangulation, \mathcal{T}^h , with the characteristic mesh size denoted by h . Consequently, the discretization of the solution fields in Eq. (1) using FE basis is given by $u^{\beta,h}(\mathbf{x}) = \sum_{j=1}^m u_j^\beta N_j^h(\mathbf{x})$ with u_j^β denoting the coefficients of the β^{th} discretized field for $\beta = 1, 2, \dots, n_v$.

Applying the above finite-element discretization to the boundary value problem (Eq. (1)) results in the following matrix equations to be solved for the FE nodal degrees of freedom (DoF)

$\mathbf{u}^\beta \in \mathbb{R}^m \quad \forall \beta = 1, \dots, n_v$:

$$\begin{aligned} \mathbf{K}\mathbf{u}^\beta + \mathbf{M}^\kappa \mathbf{u}^\beta &= \begin{cases} \mathbf{f}^\beta \\ \lambda_\beta \mathbf{M}\mathbf{u}^\beta \end{cases} \\ \mathbf{u}_J^\beta &= \Pi u_D(\mathbf{x}_J) \quad \forall \mathbf{x}_J \in \partial\Omega_D \end{aligned} \quad (2)$$

with \mathbf{K} , \mathbf{M}^κ , \mathbf{M} , \mathbf{f}^i denoting the stiffness matrix, weighted stiffness matrix, mass matrix and the forcing vector respectively, and are defined as:

$$\begin{aligned} K_{IJ} &= \int_{\Omega} \mu \nabla N_I^h(\mathbf{x}) \cdot \nabla N_J^h(\mathbf{x}) d\mathbf{x} & M_{IJ}^\kappa &= \int_{\Omega} \kappa(\mathbf{x}) N_I^h(\mathbf{x}) N_J^h(\mathbf{x}) d\mathbf{x} \\ M_{IJ} &= \int_{\Omega} N_I^h(\mathbf{x}) N_J^h(\mathbf{x}) d\mathbf{x} & f_I^\beta &= \int_{\Omega} N_I^h(\mathbf{x}) f^\beta(\mathbf{x}) d\mathbf{x} \end{aligned}$$

Defining the multi-vectors $\mathbf{U} = [\mathbf{u}^1 \ \mathbf{u}^2 \ \dots \ \mathbf{u}^{n_v}]$ and $\mathbf{F} = [\mathbf{f}^1 \ \mathbf{f}^2 \ \dots \ \mathbf{f}^{n_v}]$, we can now rewrite Eq. (2) as

$$\begin{aligned} \mathbf{K}\mathbf{U} + \mathbf{M}^\kappa \mathbf{U} &= \begin{cases} \mathbf{F} \\ \mathbf{M}\mathbf{U}\mathbf{A} \end{cases} \\ U_{J\beta} &= \Pi u_D(\mathbf{x}_J) \quad \forall \mathbf{x}_J \in \partial\Omega_D \end{aligned} \quad (3)$$

where $\Lambda_{\alpha\beta} = \delta_{\alpha\beta} \lambda_\alpha$.

The computational efficiency of an iterative solution strategy to solve the linear system of equations or the eigenvalue problem in Eq. (3) relies on the efficient evaluation of matrix multi-vector products $\mathbf{K}\mathbf{U}$, $\mathbf{M}^\kappa \mathbf{U}$ and $\mathbf{M}\mathbf{U}$, which will be the primary focus of this work.

2.2. Matrix multi-vector product

According to the standard prescription of finite-element discretization, we assume a non-overlapping partition of Ω into finite-elements $\Omega^{(e)}$, i.e., $\Omega = \bigcup_{e=1}^E \Omega^{(e)}$ where E is the number of finite-elements. We refer to these elements $\Omega^{(e)}$ as FE cells, and in this work, we choose them to be hexahedral finite-elements. Furthermore, we assume that a linear map exists from each FE cell to a reference domain $\hat{\Omega} = [-1, 1]^3$ with $\xi = [\xi_1, \xi_2, \xi_3]$ as the reference coordinate system. In this framework, the discretized field $u^{\beta,h}(\mathbf{x})$ in a given FE cell (e) can be defined in the following way:

$$\begin{aligned} u^{\beta,h(e)}(\mathbf{x}(\xi)) &= \sum_{J=1}^{n_p^3} u^{\beta,h(e)}(\mathbf{x}_J^{(e)}) \hat{N}_J(\xi) \\ &= \sum_{j_1=1}^{n_p} \sum_{j_2=1}^{n_p} \sum_{j_3=1}^{n_p} u^{\beta,h(e)}(\mathbf{x}_{j_1 j_2 j_3}^{(e)}) \hat{N}_{j_1}^{1D}(\xi^1) \hat{N}_{j_2}^{1D}(\xi^2) \hat{N}_{j_3}^{1D}(\xi^3) \end{aligned} \quad (4)$$

where \hat{N}_J is the 3D finite-element (FE) cell-level basis function corresponding to the FE node J . Further, the tensor structured nature of $\hat{N}_J(\xi)$ is exploited in Eq. (4) to express it as the product of three 1D Lagrange interpolating polynomials of order FEOrder = $n_p - 1$, defined on the Gauss Legendre Lobatto nodal points in $[-1, 1]$, with n_p denoting the number of points in each direction, while $\mathbf{x}_{j_1 j_2 j_3}^{(e)}$ is the cartesian coordinate of the node J indexed by j_1, j_2, j_3 in $\Omega^{(e)}$.

In order to make the problem more amenable to distributed parallelism, we partition the domain Ω into subdomains $\Omega^t \ \forall t = 1, 2, \dots, n_t$, where n_t is the number of subdomains, and assign each subdomain $\Omega^{(t)}$ to an MPI task t . Let E_t be the number of FE cells, and m_t be the number of basis functions in each subdomain $\Omega^{(t)}$ such that $\Omega^{(t)} = \bigcup_{e=1}^{E_t} \Omega^{(e)}$. Consequently, the matrix-multi-vector product $\mathbf{A}\mathbf{U}$, where \mathbf{A} denotes the FE discretized matrix (such as \mathbf{K} , \mathbf{M}^κ , \mathbf{M} or $\mathbf{K} + \mathbf{M}^\kappa$), can be written as follows:

$$\mathbf{V} = \mathbf{A}\mathbf{U} = \left[\sum_t \mathbf{P}^{(t)T} \mathbf{C}^{(t)T} \left(\sum_e \mathbf{Q}^{(e,t)T} \mathbf{A}^{(e)} \mathbf{Q}^{(e,t)} \right) \mathbf{C}^{(t)} \mathbf{P}^{(t)} \right] \mathbf{U} \quad (5)$$

where the multi-index (e, t) denotes the FE cell index (e) associated with a MPI task (t) and $\mathbf{P}^{(t)}$ denotes the partitioner matrix whose action on \mathbf{U} gives the subdomain level multi-vector \mathbf{U}^t . The condition that $u^{\beta,h}(\mathbf{x})$ needs to be continuous across the partitioned subdomains is imposed by this Boolean sparse matrix \mathbf{P}^t . Further $\mathbf{C}^{(t)}$ in Eq. (5) denotes a $m_t \times m_t$ constraint matrix employed to constrain the values of the $M \times n_v$ matrix \mathbf{U} at certain nodes. These constraints are used to either satisfy the necessary boundary conditions imposed on $u^{\beta,h}(\mathbf{x})$ or to deal with constraints arising from non-conforming meshes. Furthermore, imposition of continuity condition associated with $u^{\beta,h}(\mathbf{x})$ across FE cells within a partitioned subdomain $\Omega^{(t)}$ is accomplished by the action of $n_p^3 \times m_t$ Boolean sparse matrix $\mathbf{Q}^{(e,t)}$ on the constrained subdomain level multi-vector $\mathbf{C}^{(t)} \mathbf{P}^{(t)} \mathbf{U}$, with $\mathbf{Q}^{(e,t)}$ representing the subdomain to FE cell level map on the subdomain Ω_t . Finally, the FE cell-level matrix $\mathbf{A}^{(e)}$ arising from the finite-element discretization of the underlying PDE can be evaluated as an integral over the reference domain $\hat{\Omega}$. For instance, the $n_p^3 \times n_p^3$ cell-level matrix $\mathbf{K}^{(e)}$ associated with the matrix \mathbf{K} in Eq. (3) can be evaluated as

$$K_{IJ}^{(e)} = \int_{\Omega^{(e)}} \mu \nabla N_I \cdot \nabla N_J d\mathbf{x} \quad (6a)$$

$$= \int_{\hat{\Omega}} \mu \left(\mathbf{J}^{(e)-T} \nabla_\xi \hat{N}_I \right) \cdot \left(\mathbf{J}^{(e)-T} \nabla_\xi \hat{N}_J \right) \det \mathbf{J}^{(e)} d\hat{\mathbf{x}} \quad (6b)$$

$$= \sum_{Q=1}^{n_q^3} \left(\nabla_\xi \hat{N}_I \right)^T \mathbf{J}^{(e)-1} \mathbf{J}^{(e)-T} \left(\nabla_\xi \hat{N}_J \right) \mu w_Q \det \mathbf{J}^{(e)} \Big|_{\xi_Q} \quad (6c)$$

where $\nabla_\xi \hat{N}_I$ denotes the gradient of the FE cell-level basis function within reference coordinate system ξ , while $\mathbf{J}^{(e)}$ denotes the Jacobian matrix of the map from $\Omega^{(e)}$ to $\hat{\Omega}$. Furthermore, a tensor structured n_q -point quadrature rule with quadrature points ξ_Q and the quadrature weights w_Q is used in evaluating the integral involved in Eq. (6b). Note that the tensor structured nature of the quadrature rule allows us to write the 3D quadrature weights as the product of 1D quadrature weights $w_Q = w_{q_1}^{1D} w_{q_2}^{1D} w_{q_3}^{1D}$ where w_q^{1D} with $q = 1, \dots, n_q$ are the quadrature weights of the 1D quadrature rule.

Defining $D_{QI}^s = \nabla_\xi \hat{N}_I(\xi_Q) \cdot \hat{\mathbf{n}}_s$ as $n_q^3 \times n_p^3$ matrices where $\hat{\mathbf{n}}_s$, $s = 0, 1, 2$ represents the unit vector along the s axis, we can now rewrite Eq. (6c) as

$$\mathbf{K}^{(e)} = \begin{bmatrix} \mathbf{D}^{(0)} \\ \mathbf{D}^{(1)} \\ \mathbf{D}^{(2)} \end{bmatrix}^T \begin{bmatrix} \mathcal{G}^{(0,0)} & \mathcal{G}^{(0,1)} & \mathcal{G}^{(0,2)} \\ \mathcal{G}^{(1,0)} & \mathcal{G}^{(1,1)} & \mathcal{G}^{(1,2)} \\ \mathcal{G}^{(2,0)} & \mathcal{G}^{(2,1)} & \mathcal{G}^{(2,2)} \end{bmatrix} \begin{bmatrix} \mathbf{D}^{(0)} \\ \mathbf{D}^{(1)} \\ \mathbf{D}^{(2)} \end{bmatrix} \quad (7)$$

where $\mathcal{G}^{(s,d)}$ for $s, d = 0, 1, 2$ are $n_q^3 \times n_q^3$ diagonal matrices with the diagonal entry $\mathcal{G}_{QQ}^{(s,d)} = \left[\left(\mathbf{J}^{(e)} \right)^{-1} \left(\mathbf{J}^{(e)} \right)^{-T} \right]_{sd} \det \mathbf{J}^{(e)} \mu_{w_Q} \Big|_{\hat{\mathbf{x}}_Q}$. We can rewrite the weighted mass matrix in the same framework as

$$\mathbf{M}^{\kappa,(e)} = \mathbf{N}^T \mathcal{G} \mathbf{N} \quad (8)$$

where $N_{QI} = \hat{N}_I(\hat{\xi}_Q)$ is an $n_q^3 \times n_p^3$ matrix and $\mathcal{G}_{QQ} = \kappa \det \mathbf{J}^{(e)} w_Q \Big|_{\hat{\xi}_Q}$ is an $n_q^3 \times n_q^3$ matrix. We obtain the unweighted mass matrix $\mathbf{M}^{(e)}$ by setting $\kappa = 1$.

A straightforward approach to evaluate the matrix-multi-vector product $\mathbf{V} = \mathbf{A}\mathbf{U}$ is to construct the *global FE discretized matrix* \mathbf{A} as outlined in Eq. (5) and perform the sparse-matrix dense-matrix product. However, this method does not exploit the known properties of \mathbf{A} and is computationally less efficient when compared to the alternative methods discussed below.

Similar to the strategy used for FE-discretized matrix-single vector multiplication, we now present two computationally efficient methods for evaluating the matrix-multi-vector product $\mathbf{V} = \mathbf{A}\mathbf{U}$.

2.2.1. Evaluation -via- FE-cell level local dense matrices

The matrix multi-vector product $\mathbf{V} = \mathbf{A}\mathbf{U}$ can be evaluated using the FE-cell level matrices $\mathbf{A}^{(e)}$ and the FE-cell level multi-vectors as follows:

1. **Precompute** the FE-cell level operator matrices $\mathbf{A}^{(e)}$
2. **Extraction** of the FE-cell level multi-vectors $\mathbf{U}^{(e,t)}$ using the *subdomain to FE-cell level map*, the *constraint* and the *partitioner* matrices, i.e., $\mathbf{U}^{(e,t)} = \mathbf{Q}^{(e,t)} \mathbf{C}^{(t)} \mathbf{P}^{(t)} \mathbf{U} \forall e = 1, 2, \dots, E_t$
3. **FE-cell level evaluation** of the matrix vector product $\mathbf{V}^{(e,t)} = \mathbf{A}^{(e)} \mathbf{U}^{(e,t)}$ using batched matrix-matrix multiplication.
4. **Assembly** of the global multi-vector \mathbf{V} using the *subdomain to FE-cell level map*, the *constraint* and the *partitioner* matrices.

We can mathematically represent the above steps in the matrix-multi-vector product as:

$$\mathbf{V} = \mathbf{A}\mathbf{U} = \left[\sum_t \mathbf{P}^{(t)T} \mathbf{C}^{(t)T} \sum_e \left(\mathbf{Q}^{(e,t)T} \mathbf{A}^{(e)} \mathbf{U}^{(e,t)} \right) \right] \quad (9)$$

where $\mathbf{U}^{(e,t)} = \mathbf{Q}^{(e,t)} \mathbf{C}^{(t)} \mathbf{P}^{(t)} \mathbf{U}$ denotes FE-cell level multi-vectors extracted from the global multi-vector \mathbf{U} defined on the domain Ω . The cost of the precompute step is amortized over multiple evaluations of the matrix multi-vector products usually encountered in iterative algorithms. In this framework, the FE-cell level evaluation is the computationally dominant step with the computational complexity of $O(En_p^6 n_v)$. Furthermore, since this method requires us to store the FE-cell level matrices and multi-vectors, the resulting memory footprint is $O(En_p^6 + En_p^3 n_v)$.

2.2.2. Evaluation -via- matrix-free approach

In the matrix-free approach, which will be the primary focus of this work, we avoid the precomputation of the FE-cell level

matrices $\mathbf{A}^{(e)}$. Instead, the FE-cell level matrix multi-vector products $\mathbf{A}^{(e)} \mathbf{U}^{(e,t)}$ are evaluated *on-the-fly*. Using the expressions in Eqs. (7) and (8) we observe that first step in evaluating $\mathbf{A}^{(e)} \mathbf{U}^{(e,t)} = \left(\mathbf{K}^{(e)} + \mathbf{M}^{\kappa,(e)} \right) \mathbf{U}^{(e,t)}$ involves computing the action of \mathbf{D}^k and \mathbf{N} on $\mathbf{U}^{(e,t)}$. To this end, we exploit the tensor-structured nature of the FE basis functions and the quadrature rules. Treating the FE-cell level multi-vector $\mathbf{U}^{(e,t)}$ as a 4th order tensor, $\mathbf{U}_{\beta,j_1,j_2,j_3}^{(e,t)} = u^{\beta,h,(e)} \left(\mathbf{x}_{j_1,j_2,j_3}^{(e)} \right)$, with one dimension corresponding to the vector index (β) and the other three corresponding to the spatial indices (j_1, j_2, j_3), we can represent the action of \mathbf{D}^k and \mathbf{N} on $\mathbf{U}^{(e,t)}$ as

$$\mathbf{N}\mathbf{U}^{(e,t)} \equiv \left(\mathbf{N}^{1D} \otimes \mathbf{N}^{1D} \otimes \mathbf{N}^{1D} \otimes \mathbf{I} \right) \mathbf{U}^{(e,t)} \quad (10)$$

$$\begin{bmatrix} \mathbf{D}^{(0)} \\ \mathbf{D}^{(1)} \\ \mathbf{D}^{(2)} \end{bmatrix} \mathbf{U}^{(e,t)} \equiv \begin{bmatrix} \mathbf{N}^{1D} \otimes \mathbf{N}^{1D} \otimes \mathbf{D}^{1D} \otimes \mathbf{I} \\ \mathbf{N}^{1D} \otimes \mathbf{D}^{1D} \otimes \mathbf{N}^{1D} \otimes \mathbf{I} \\ \mathbf{D}^{1D} \otimes \mathbf{N}^{1D} \otimes \mathbf{N}^{1D} \otimes \mathbf{I} \end{bmatrix} \mathbf{U}^{(e,t)} \quad (11)$$

where \mathbf{N}^{1D} and \mathbf{D}^{1D} are $n_q \times n_p$ matrices corresponding to the one-dimensional FE basis function values and gradients, respectively, at quadrature points and \otimes represents the Kronecker product. Using the well-known result of tensor algebra, $(\mathbf{A} \otimes \mathbf{B}) = (\mathbf{I} \otimes \mathbf{B})(\mathbf{A} \otimes \mathbf{I})$ we can reduce the above expressions into a series of tensor contractions as enunciated in Algorithm 1.

Algorithm 1: Evaluation of $\mathbf{T} = \mathbf{N}\mathbf{U}^{(e,t)}$

Input: $\mathbf{U}^{(e,t)}$
Data: \mathbf{N}^{1D}
Result: \mathbf{T}

- 1 $\mathbf{T} \leftarrow \left(\mathbf{I} \otimes \mathbf{I} \otimes \mathbf{N}^{1D} \otimes \mathbf{I} \right) \mathbf{U}^{(e,t)}$;
- 2 $\mathbf{T} \leftarrow \left(\mathbf{I} \otimes \mathbf{N}^{1D} \otimes \mathbf{I} \otimes \mathbf{I} \right) \mathbf{T}$;
- 3 $\mathbf{T} \leftarrow \left(\mathbf{N}^{1D} \otimes \mathbf{I} \otimes \mathbf{I} \otimes \mathbf{I} \right) \mathbf{T}$;
- 4 **return** \mathbf{T}

In Section 3.1.4, we show that we can rewrite the tensor contractions as matrix-matrix multiplications (Eqs. (18) to (20)). Additionally, we note that \mathcal{G} and $\mathcal{G}^{(s,d)}$ are diagonal matrices, and we can evaluate their action on $\mathbf{N}\mathbf{U}^{(e,t)}$ and $\mathbf{D}^k \mathbf{U}^{(e,t)}$ as point-wise multiplications. Finally, we compute the action of \mathbf{D}^{kT} and \mathbf{N}^T in the same way as the action of \mathbf{D}^k and \mathbf{N} . With this framework, if we assume that \mathcal{G} and $\mathcal{G}^{(s,d)}$ are precomputed, the computational complexity of evaluating $\mathbf{M}^{\kappa,(e)} \mathbf{U}^{(e,t)}$ is $O((4(n_p^3 n_q + n_p^2 n_q^2 + n_p n_q^3) + n_q^3) n_v)$ and the computational complexity of evaluating $\mathbf{K}^{(e)} \mathbf{U}^{(e,t)}$ is $O((12(n_p^3 n_q + n_p^2 n_q^2 + n_p n_q^3) + 3n_q^3) n_v)$.

Alternatively, we can evaluate $\mathbf{K}^{(e)} \mathbf{U}^{(e)}$ by expressing $\hat{N}_i^{1D}(\xi)$ as $\hat{N}_i^{1D}(\xi) = \sum_{\hat{q}} \hat{N}_i^{1D}(\hat{x}_{\hat{q}}) \tilde{N}_{\hat{q}}^{1D}(\xi)$ where $\tilde{N}_{\hat{q}}^{1D}$ are the Lagrange polynomials defined at the quadrature points. This allows us to write $\frac{d\hat{N}_i^{1D}(\xi)}{d\xi} = \sum_{\hat{q}} \hat{N}_i^{1D}(\hat{x}_{\hat{q}}) \frac{d\tilde{N}_{\hat{q}}^{1D}(\xi)}{d\xi}$. Consequently, we can now factorize \mathbf{D}^{1D} as $\mathbf{D}^{1D} = \tilde{\mathbf{D}}^{1D} \mathbf{N}^{1D}$ where $\tilde{D}_{\hat{q}\hat{q}}^{1D} = \left. \frac{d\tilde{N}_{\hat{q}}^{1D}(\xi)}{d\xi} \right|_{\hat{x}_{\hat{q}}}$.

Equation (11) can now be rewritten as

$$\begin{bmatrix} \mathbf{D}^{(0)} \\ \mathbf{D}^{(1)} \\ \mathbf{D}^{(2)} \end{bmatrix} \mathbf{U}^{(e,t)} = \begin{bmatrix} \mathbf{I} \otimes \mathbf{I} \otimes \tilde{\mathbf{D}}^{1D} \otimes \mathbf{I} \\ \mathbf{I} \otimes \tilde{\mathbf{D}}^{1D} \otimes \mathbf{I} \otimes \mathbf{I} \\ \tilde{\mathbf{D}}^{1D} \otimes \mathbf{I} \otimes \mathbf{I} \otimes \mathbf{I} \end{bmatrix} \mathbf{N} \mathbf{U}^{(e,t)} = \begin{bmatrix} \tilde{\mathbf{D}}^{(0)} \\ \tilde{\mathbf{D}}^{(1)} \\ \tilde{\mathbf{D}}^{(2)} \end{bmatrix} \mathbf{N} \mathbf{U}^{(e,t)} \quad (12)$$

Using this factorization, the evaluation of $\mathbf{K}^{(e)} \mathbf{U}^{(e,t)}$ can be done with a computational complexity of $O((4(n_p^3 n_q + n_p^2 n_q^2 + n_p n_q^3) + 12n_q^4 + 3n_q^3 n_v))$. Note that this approach reduces the floating point operations required when $n_q = n_p$ by $\sim 30\%$. Even in the case of $n_q > n_p$, this factorization is beneficial while evaluating the action of $\mathbf{A}^{(e)} = \mathbf{K}^{(e)} + \mathbf{M}^{\kappa(e)}$ as it allows us to reduce the number of required tensor contraction by factorizing out \mathbf{N} and \mathbf{N}^T

$$\begin{aligned} \mathbf{A}^{(e)} \mathbf{U}^{(e,t)} &= (\mathbf{K}^{(e)} + \mathbf{M}^{\kappa(e)}) \mathbf{U}^{(e,t)} \\ &= \mathbf{N}^T \left(\begin{bmatrix} \tilde{\mathbf{D}}^{(0)} \\ \tilde{\mathbf{D}}^{(1)} \\ \tilde{\mathbf{D}}^{(2)} \end{bmatrix}^T \begin{bmatrix} \mathcal{G}^{(0,0)} & \mathcal{G}^{(0,1)} & \mathcal{G}^{(0,2)} \\ \mathcal{G}^{(1,0)} & \mathcal{G}^{(1,1)} & \mathcal{G}^{(1,2)} \\ \mathcal{G}^{(2,0)} & \mathcal{G}^{(2,1)} & \mathcal{G}^{(2,2)} \end{bmatrix} \begin{bmatrix} \tilde{\mathbf{D}}^{(0)} \\ \tilde{\mathbf{D}}^{(1)} \\ \tilde{\mathbf{D}}^{(2)} \end{bmatrix} + \mathcal{G} \right) \mathbf{N} \mathbf{U}^{(e,t)} \end{aligned} \quad (13)$$

Using Eq. (13), we write the algorithm for the evaluation of $\mathbf{V}^{(e)}$ in the case of $\mathbf{A}^{(e)} = \mathbf{K}^{(e)} + \mathbf{M}^{\kappa(e)}$ in Algorithm 2.

Algorithm 2: Evaluation of $\mathbf{V}^{(e,t)} = (\mathbf{K}^{(e)} + \mathbf{M}^{\kappa(e)}) \mathbf{U}^{(e,t)}$	
Input: $\mathbf{U}^{(e,t)}$	
Data: $\mathbf{N}^{1D}, \tilde{\mathbf{D}}^{1D}, \mathcal{G}, \mathcal{G}^{(s,d)}$ where $s, d = 0, 1, 2$	
Temporary Variables: $\mathbf{T}, \mathbf{T}^{(0)}, \mathbf{T}^{(1)}, \mathbf{T}^{(2)}$	
Result: $\mathbf{V}^{(e,t)}$	
1	$\mathbf{T} \leftarrow \mathbf{N} \mathbf{U}^{(e,t)};$ // Algorithm 1
2	$\mathbf{T}^{(0)} \leftarrow (\mathbf{I} \otimes \mathbf{I} \otimes \tilde{\mathbf{D}}^{1D} \otimes \mathbf{I}) \mathbf{T};$
3	$\mathbf{T}^{(1)} \leftarrow (\mathbf{I} \otimes \tilde{\mathbf{D}}^{1D} \otimes \mathbf{I} \otimes \mathbf{I}) \mathbf{T};$
4	$\mathbf{T}^{(2)} \leftarrow (\tilde{\mathbf{D}}^{1D} \otimes \mathbf{I} \otimes \mathbf{I} \otimes \mathbf{I}) \mathbf{T};$
5	$\mathbf{T}_s \leftarrow \sum_{d=0}^2 \mathcal{G}^{(s,d)} \mathbf{T}_d;$
6	$\mathbf{T} \leftarrow \mathcal{G} \mathbf{T};$
7	$\mathbf{T} \leftarrow \mathbf{T} + (\mathbf{I} \otimes \mathbf{I} \otimes \tilde{\mathbf{D}}^{1D} \otimes \mathbf{I})^T \mathbf{T}^{(0)};$
8	$\mathbf{T} \leftarrow \mathbf{T} + (\mathbf{I} \otimes \tilde{\mathbf{D}}^{1D} \otimes \mathbf{I} \otimes \mathbf{I})^T \mathbf{T}^{(1)};$
9	$\mathbf{T} \leftarrow \mathbf{T} + (\tilde{\mathbf{D}}^{1D} \otimes \mathbf{I} \otimes \mathbf{I} \otimes \mathbf{I})^T \mathbf{T}^{(2)};$
10	$\mathbf{V}^{(e,t)} \leftarrow \mathbf{N}^T \mathbf{T};$ // Algorithm 1
11	return $\mathbf{V}^{(e,t)}$

3. Hardware aware implementation of the Matrix-free formulation

This section describes the proposed hardware-aware implementation procedures for evaluating FE discretized matrix-multi-vector products using the matrix-free approach on multinode CPU and GPU architectures. To this end, consider the global

multi-vector \mathbf{U} of size $n_v \times m$. In the extraction step, the FE-cell-level multi-vectors $\mathbf{U}^{(e,t)}$ of size $n_v \times n_p^3$ are constructed from \mathbf{U} using the *subdomain to FE-cell level map* and the *partitioner*. The FE-cell-level evaluation in the matrix-free framework involves tensor contractions (Eq. (13)) and a point-wise multiplication to represent the action of \mathcal{G} and \mathcal{G}_{ij} . After the FE-cell level evaluation, the output FE-cell level matrices $\mathbf{V}^{(e,t)}$ are assembled back into the output node-level multi-vector \mathbf{V} employing the same map and partitioner used in the extraction phase. We describe more implementation details about this procedure in the following subsections.

3.1. Batched Evaluation Strategy

The traditional approach for evaluating the matrix-vector product involves multiplying the FE-discretized operator with all the constituent vectors of the multi-vector concurrently [3, 21]. However, for the matrix-free approach, we find that this approach is inefficient. A more efficient strategy involves selectively processing a smaller number of vectors concurrently, with the number of vectors tailored to hardware architectures, such as the SIMD vectorization width in CPUs or the shared memory size on GPUs. To facilitate analysis, we define b to be the number of vectors in a given batch, $n_b = \lceil n_v / b \rceil$ to be the number of batches, and boolean sparse matrices $\mathbf{B}^{(i_b)}$, which act on the multi-vector and extract a single batch (i_b) of vectors.

CPU Batched Strategy

In this framework, in the case of CPUs, Eq. (5) is rewritten as

$$\mathbf{V} = \sum_{i_b} \mathbf{B}^{(i_b)T} \left(\sum_t \mathbf{P}^{(i_b,t)T} \mathbf{C}^{(i_b,t)T} \left(\sum_e \mathbf{Q}^{(i_b,e,t)T} \mathbf{A}^{(e)} \mathbf{Q}^{(i_b,e,t)} \right) \mathbf{C}^{(i_b,t)} \mathbf{P}^{(i_b,t)} \right) \mathbf{B}^{(i_b)} \mathbf{U} \quad (14)$$

Here, $\mathbf{P}^{(i_b,t)}$ represents the partitioner matrix which acts on a single batch (i_b) of the multi-vector, $\mathbf{U}^{(i_b)} = \mathbf{B}^{(i_b)} \mathbf{U}$, and extracts the multi-vector belonging to the subdomain Ω^t (on MPI task t). The constraint matrix, $\mathbf{C}^{(i_b,t)}$, then acts on the result to ensure that all the constraints are satisfied, resulting in $\mathbf{U}^{(i_b,t)} = \mathbf{C}^{(i_b,t)} \mathbf{P}^{(i_b,t)} \mathbf{B}^{(i_b)} \mathbf{U}$, which is the multi-vector corresponding to batch i_b and subdomain Ω^t . The *subdomain to FE-cell level map*, $\mathbf{Q}^{(i_b,e,t)}$, then acts on this subdomain level multi-vector batch resulting in the FE-cell level multi-vector batch $\mathbf{U}^{(i_b,e,t)} = \mathbf{Q}^{(i_b,e,t)} \mathbf{U}^{(i_b,t)}$. We evaluate the FE-cell level product as $\mathbf{V}^{(i_b,e,t)} = \mathbf{A}^{(e)} \mathbf{U}^{(i_b,e,t)}$. We then map this FE-cell level product to the subdomain level product multi-vector via the transpose of the *subdomain to FE-cell level map* and then sum over the contributions from all the FE-cells belonging to Ω^t . The transpose of the constraint matrix then acts on the result to ensure that the constraints are satisfied, resulting in $\mathbf{V}^{(i_b,t)} = \mathbf{C}^{(i_b,t)T} \left(\sum_e \mathbf{Q}^{(i_b,e,t)T} \mathbf{V}^{(i_b,e,t)} \right)$, which is the product multi-vector corresponding to batch i_b and subdomain Ω^t . The transpose of the partitioner acts on this subdomain level product multi-vector batch to return the global product multi-vector batch, and we sum over all the subdomains, $\mathbf{V}^{(i_b)} = \sum_t \mathbf{P}^{(i_b,t)T} \mathbf{V}^{(i_b,t)}$. This process is repeated for every batch, $\mathbf{V} = \sum_{i_b} \mathbf{B}^{(i_b)T} \mathbf{V}^{(i_b)}$.

GPU Batched Strategy:

In contrast to batched evaluation on CPU architectures, we need to rewrite Eq. (5) to better harness the parallelism of GPU architectures by further parallelizing over both FE-cells and batches. To this end, we interchange the order of the operations and consequently rewrite Eq. (5) as

$$\mathbf{V} = \sum_t \mathbf{P}^{(t)T} \mathbf{C}^{(t)T} \left(\sum_{i_b} \sum_e \mathbf{B}^{(i_b,t)T} \mathbf{Q}^{(i_b,e,t)T} \mathbf{A}^{(e)} \mathbf{Q}^{(i_b,e,t)} \mathbf{B}^{(i_b,t)} \right) \mathbf{C}^{(t)} \mathbf{P}^{(t)} \mathbf{U} \quad (15)$$

Here $\mathbf{P}^{(t)}$ represents the partitioner which acts on \mathbf{U} and extracts the multi-vector $\mathbf{U}^{(t)} = \mathbf{P}^{(t)} \mathbf{U}$, belonging to the subdomain Ω^t (on MPI task t). $\mathbf{C}^{(t)}$ represents the constraint matrix which then acts on $\mathbf{U}^{(t)}$, updating it and ensuring that all the constraints are satisfied. Then the operators $\mathbf{B}^{(i_b,t)}$, $\mathbf{Q}^{(i_b,e,t)}$ and $\mathbf{A}^{(e)}$ act in sequence to evaluate the FE-cell level output $\mathbf{V}^{(i_b,e,t)} = \mathbf{A}^{(e)} \mathbf{Q}^{(i_b,e,t)} \mathbf{B}^{(i_b,t)} \mathbf{U}^{(t)}$. Here $\mathbf{B}^{(i_b,t)}$ represents the extraction of batch i_b for subdomain Ω^t and $\mathbf{Q}^{(i_b,e,t)}$ represents the *subdomain to FE-cell level map* for the FE-cell identified by e , batch i_b and task t . We then map the FE-cell level product to the subdomain level product multi-vector via the transpose of the *subdomain to FE-cell level map* using $\mathbf{Q}^{(i_b,e,t)T}$. We do this for every batch using $\mathbf{B}^{(i_b,t)T}$ and then sum over the contribution from all the FE-cells and batches of vectors belonging to Ω^t to form $\mathbf{V}^{(t)}$. We perform these operations required for evaluation $\mathbf{V}^{(t)}$ concurrently for every FE-cell and batch through a single kernel launch, and thus the summations over indices i_b and e occur concurrently. The transpose of the constraint matrix $\mathbf{C}^{(t)T}$, then acts on $\mathbf{V}^{(t)}$ to ensure that the constraints are satisfied and updates it. Finally, the transpose of the partitioner $\mathbf{P}^{(t)T}$, acts on this subdomain level product multi-vector $\mathbf{V}^{(t)}$ to return the global product multi-vector \mathbf{V} . We will discuss these operations in more detail in the upcoming sections.

3.1.1. Data Layout: Storage of $\mathbf{U}^{(t)}$

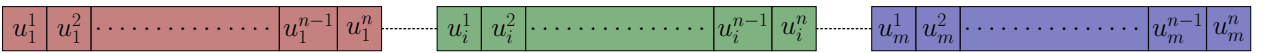
We do not explicitly store the global multi-vector \mathbf{U} . Instead each MPI task t stores the subdomain level multi-vector $\mathbf{U}^{(t)}$ and the action of the partitioner, $\mathbf{P}^{(t)}$ ($\mathbf{P}^{(i_b,t)}$ on CPU architectures), on \mathbf{U} ($\mathbf{U}^{(i_b)}$ on CPU architectures) is evaluated via MPI communication across tasks possessing neighboring subdomains. A data layout for storing the subdomain level multi-vector $\mathbf{U}^{(t)}$ involves storing the FE nodal values of all the constituent vectors in a contiguous fashion allowing for memory-efficient access to all the vectors at a given node. Das et al. [3, 21] have demonstrated

excellent throughput performance on both CPUs and GPUs utilizing this data layout for the FE discretized eigenvalue problem arising in quantum modeling of materials -via- the FE-cell level local dense matrix approach. We term this layout the *Contiguous Vector (CV)* layout. For the matrix-free approach, as discussed above, we perform the computations more efficiently if the number of vectors simultaneously dealing with a given FE node is tailored to hardware architectures. To this end, we propose a batched layout for storing the multi-vector. This layout termed the *Batched Contiguous Vector (BCV)* layout, stores the nodal values of a batch of b vectors in a contiguous fashion for all the nodes and repeats itself for the $n_b = \lceil n/b \rceil$ batches. We illustrate the layouts in Fig. 1 and discuss the performance improvements in the subsequent sections.

3.1.2. Applying the constraints: Action of $\mathbf{C}^{(t)}$ and $\mathbf{C}^{(t)T}$

We now discuss the application of constraints, mathematically represented as the application of sparse matrices $\mathbf{C}^{(t)}$ and $\mathbf{C}^{(t)T}$ ($\mathbf{C}^{(i_b,t)}$ and $\mathbf{C}^{(i_b,t)T}$ in case of CPU architectures) as discussed in Section 2.2. We note that the most commonly encountered constraints in non-conforming adaptively refined meshes are the hanging-node constraints [23], which are locally dense, as they involve interpolation along faces/edges. Consequently, we adopt a local dense matrix approach for applying constraints. We store the constraints as multiple sets, where each set contains four vectors and represents all the constraints that involve the same master nodes. The four vectors include a vector containing master node indices, a vector containing all the slave node indices, a vector consisting of the weight matrix for this set of constraints, and a vector containing the inhomogeneities corresponding to the slave nodes. For the application of $\mathbf{C}^{(t)}$ on a given batch of vectors, we read the nodal values corresponding to the master nodes of a batch of the multi-vector into a temporary matrix. We multiply this matrix with the weight matrix, a dense matrix-matrix product, and add the inhomogeneity vector to the result. Then we write the result back to slave nodes of the multi-vector corresponding to the same batch. We also evaluate the action of $\mathbf{C}^{(t)T}$ similarly. We also apply the Dirichlet boundary conditions using the same framework. For Dirichlet constraints, the master index vector and weight matrix vector are empty. In this format, the application of constraints, a sparse matrix multiplication, reduces to a sequence of dense matrix-matrix multiplications. Recently Munch et al. [24] proposed a matrix-free method for resolving the hanging node constraints, which will likely be more efficient than our implementation and

Contiguous Vector (CV) Layout



Batched Contiguous Vector (BCV) Layout

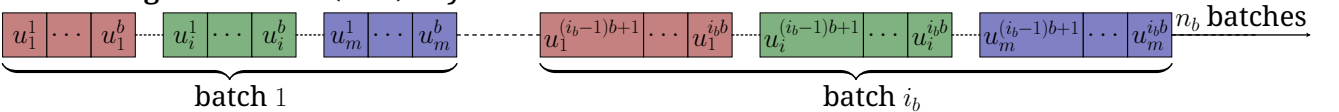


Figure 1: Pictorial depiction of the layouts described in Section 3.1.1. Here $u_j^\beta = u^\beta(\mathbf{x}_j)$ with β representing the vector index and j representing the spatial index.

requires further investigation.

3.1.3. Extraction and Assembly: Action of $\mathbf{Q}^{(i_b, e, t)}$ and $\mathbf{Q}^{(i_b, e, t)T}$

The action of the Boolean sparse matrix $\mathbf{Q}^{(i_b, e, t)}$ on the subdomain level multi-vector batch $\mathbf{U}^{(i_b, t)}$ to extract the FE-cell level multi-vector batch $\mathbf{U}^{(i_b, e, t)}$ can be viewed as a discontinuous read from $\mathbf{U}^{(i_b, t)}$ of the data corresponding to the nodes within Ω^e . Thus, the action of $\mathbf{Q}^{(i_b, e, t)}$ on $\mathbf{U}^{(i_b, t)}$ is implemented as a straightforward discontinuous read. Similarly, we compute the action of $\mathbf{Q}^{(i_b, e, t)T}$ and the summation over e as addition into discontinuous data. The FE-cell-level multi-vector for batch i_b and FE-cell e is represented by

$$\mathbf{U}_{\text{e_ib}}[i + bp_1 + bn_p p_2 + bn_p^2 p_3] \equiv U_{i, p_1, p_2, p_3}^{(i_b, e, t)} \quad (16)$$

$$i = 1, \dots, b \quad p_1, p_2, p_3 = 1, \dots, n_p \quad (17)$$

Note that the ordering of the subscript indices represents the data contiguity in memory. We will discuss further optimizations for this step on GPUs in Section 3.1.4.

3.1.4. Tensor Contractions: Evaluation of $\mathbf{A}^{(e)}\mathbf{U}^{(i_b, e, t)}$

We will now illustrate the methodology followed for the evaluation of $\mathbf{V}^{(i_b, e, t)} = \mathbf{A}^{(e)}\mathbf{U}^{(i_b, e, t)}$ for the specific case of $\mathbf{A}^{(e)} = \mathbf{K}^{(e)} + \mathbf{M}^{\kappa^{(e)}}$ using Algorithms 1 and 2.

Note that in both Algorithms 1 and 2 we need to evaluate products of the forms $(\mathbf{I} \otimes \mathbf{I} \otimes \mathbf{A} \otimes \mathbf{I})\mathbf{U}^{(i_b, e, t)}$, $(\mathbf{I} \otimes \mathbf{A} \otimes \mathbf{I} \otimes \mathbf{I})\mathbf{U}^{(i_b, e, t)}$ and $(\mathbf{A} \otimes \mathbf{I} \otimes \mathbf{I} \otimes \mathbf{I})\mathbf{U}^{(i_b, e, t)}$ using the tensor product vec-trick, $(\mathbf{A} \otimes \mathbf{B})\text{vec}(\mathbf{X}) = \text{vec}(\mathbf{B}^T \mathbf{X} \mathbf{A})$ where $\text{vec}(\mathbf{X})$ denotes the vectorization of the matrix \mathbf{X} by stacking the columns of \mathbf{X} into a single column vector as described by Deville et al. [25], we rewrite these products as batched matrix-matrix multiplications. For instance, if $\mathbf{A} = \mathbf{N}^{1D}$, considering \mathbf{R} to be a fourth order tensor of dimensions $b \times n_p \times n_p \times n_p$ and \mathbf{T} to be a fourth order tensor of dimensions $b \times n_q \times n_q \times n_q$, we have

- $\mathbf{T} \leftarrow (\mathbf{N}^{1D} \otimes \mathbf{I} \otimes \mathbf{I} \otimes \mathbf{I})\mathbf{R}$

Treating R_{β, p_1, p_2, p_3} and T_{β, q_1, p_2, p_3} as matrices \mathbf{R} of dimensions $(bn_p^2 \times n_p)$ and \mathbf{T} of dimensions $(bn_q^2 \times n_q)$ we write

$$\mathbf{T} \leftarrow \mathbf{R}\mathbf{N}^{1DT} \quad (18)$$

- $\mathbf{T} \leftarrow (\mathbf{I} \otimes \mathbf{N}^{1D} \otimes \mathbf{I} \otimes \mathbf{I})\mathbf{R}$

Treating R_{β, p_1, p_2, p_3} and T_{β, q_1, p_2, p_3} as sets of matrices \mathbf{R}_p of dimensions $(bn_p \times n_p)$ and \mathbf{T}_p of dimensions $(bn_p \times n_q)$ where $p = 1, 2, \dots, n_p$ we write

$$\mathbf{T}_p \leftarrow \mathbf{R}_p \mathbf{N}^{1DT} \quad \forall p = 1, \dots, n_p \quad (19)$$

- $\mathbf{T} \leftarrow (\mathbf{I} \otimes \mathbf{I} \otimes \mathbf{N}^{1D} \otimes \mathbf{I})\mathbf{R}$

Treating R_{β, p_1, p_2, p_3} and T_{β, q_1, p_2, p_3} as sets of matrices \mathbf{R}_p of dimensions $(b \times n_p)$ and \mathbf{T}_p of dimensions $(b \times n_q)$ where $p = 1, 2, \dots, n_p^2$ we write

$$\mathbf{T}_p \leftarrow \mathbf{R}_p \mathbf{N}^{1DT} \quad \forall p = 1, \dots, n_p^2 \quad (20)$$

The other major part of Algorithm 2 is the evaluation of $\mathcal{G}\mathbf{T}$ and $\sum_d \mathcal{G}^{(s, d)}\mathbf{T}_d$. In order to evaluate these products we redefine the \mathbf{N}^{1D} and the $\tilde{\mathbf{D}}^{1D}$ matrices as $N_{q, p}^{1D} \leftarrow N_{q, p}^{1D} \sqrt{w_q^{1D}}$ and $\tilde{D}_{q_1, q_2}^{1D} \leftarrow \tilde{D}_{q_1, q_2}^{1D} \sqrt{w_{q_1}^{1D}/w_{q_2}^{1D}}$ where w_q^{1D} are the 1D quadrature weights as discussed in Section 2.2. This allows us to evaluate $\mathcal{G}\mathbf{T}$ and $\sum_d \mathcal{G}^{(s, d)}\mathbf{T}_d$ in the following manner

- $\mathbf{T} \leftarrow \mathcal{G}\mathbf{T}$

Considering $\kappa^{(e)}$ to be the vector of length n_q^3 defined as $\kappa_Q^{(e)} = \kappa(\mathbf{x}_Q^{(e)}) \forall Q = 1, \dots, n_q^3$ we can evaluate $\mathcal{G}\mathbf{T}$ as $\det \mathbf{J}^{(e)} \kappa \circ \mathbf{T}$ where \circ represents the batched Hadamard product defined as

$$T_{\beta, Q} \leftarrow \det \mathbf{J}^{(e)} \kappa_Q^{(e)} T_{\beta, Q} \quad \forall \beta = 1, \dots, b \quad (21)$$

Note that this reduces to matrix scaling in the case of the Helmholtz operator as $\kappa(\mathbf{x})$ is a constant.

- $\mathbf{T}^s \leftarrow \sum_d \mathcal{G}^{(s, d)}\mathbf{T}^d \forall s = 0, 1, 2$

Defining a $bn_q^3 \times 3$ matrix as $[\mathbf{T}^{(0)}\mathbf{T}^{(1)}\mathbf{T}^{(2)}]$ we can write this operation as an $bn_q^3 \times 3$ times 3×3 matrix-matrix multiplication as

$$[\mathbf{T}^{(0)}\mathbf{T}^{(1)}\mathbf{T}^{(2)}] \left((\mathbf{J}^{(e)})^{-1} (\mathbf{J}^{(e)})^{-T} \det \mathbf{J}^{(e)} \mu \right) \quad (22)$$

We now discuss the implementation of the above algorithm on CPU and GPU architectures.

CPU Implementation: Evaluation of $\mathbf{A}^{(e)}\mathbf{U}^{(i_b, e, t)}$

The implementation strategy, including constraints, extraction, and assembly performed batch-wise, used for the evaluation of $\mathbf{V}^{(i_b, t)}$ on CPU architectures is enunciated in Algorithm 3.

In order to perform the strided-batched matrix-matrix multiplications in Algorithm 3 (described by Eqs. (18) to (20)), we would need to have a function with the following signature

```
1 template <int m, int n, int k, int c, bool
   add, bool trans>
2 inline void
3 matmul(const double *A, const double *B,
   double *C)
```

Listing 1: function signature for strided batched matrix-matrix multiplication

which evaluates $\mathbf{C}_i = \mathbf{A}_i \text{op}(\mathbf{B}) + \beta \mathbf{C}_i \quad \forall i = 1, \dots, c$ where \mathbf{A}_i is a $m \times k$ matrix and $\text{op}(\mathbf{B})$ is a $k \times n$ matrix with $\beta = 1$ if $\text{add}=\text{true}$ (0 otherwise) and $\text{op}(\mathbf{B}) = \mathbf{B}^T$ if $\text{trans}=\text{true}$ (\mathbf{B} otherwise). For evaluating the batched matrix-matrix products with \mathbf{N}^{1D} and $\tilde{\mathbf{D}}^{1D}$ we explore three strategies:

1. Employ JIT modules from Intel[®] MKL version 2022.1.0 [26]. We found that for this implementation, $b = 20$ gives the best performance.
2. Handwritten matrix-matrix multiplication code using AVX-512 intrinsics to work with 8 vectors concurrently, i.e. $b = 8$.
3. Exploit the symmetry of the shape functions and quadrature points to reduce the floating point operations required by half via the *even-odd* decomposition [19, 20], and using AVX-512 intrinsics to work with eight vectors concurrently, i.e., $b = 8$. An illustration of the even-odd implementation strategy to evaluate $(\mathbf{N}^{1D} \otimes \mathbf{I} \otimes \mathbf{I} \otimes \mathbf{I})\mathbf{U}^{(i_b, e, t)}$ in Fig. 3 and Listing 2.

The results of our explorations can be inferred from Fig. 2. We find that *even-odd* decomposition approach gives the best performance. We also note that the BCV layout significantly augments the performance of all three implementations.

Algorithm 3: Batchwise evaluation of \mathbf{V} on CPUs

Input: \mathbf{U}
Data: $\mathbf{B}^{(i_b)}$, $\mathbf{P}^{(i_b,t)}$, $\mathbf{C}^{(i_b,t)}$, $\mathbf{Q}^{(i_b,e,t)}$, \mathbf{N}^{1D} , \mathbf{D}^{1D} , \mathbf{J}^e , κ
Temporary Variables: \mathbf{T} , $\mathbf{T}^{(0)}$, $\mathbf{T}^{(1)}$, $\mathbf{T}^{(2)}$
Result: \mathbf{V}
MPI rank: t

- 1 $\mathbf{U}^{(i_b,t)} \leftarrow \mathbf{C}^{(i_b,t)} \mathbf{U}^{(i_b,t)}$; // Section 3.1.2
- 2 **for** $e \leftarrow 1$ **to** E_t **do**
- 3 $\mathbf{T} \leftarrow \mathbf{Q}^{(i_b,e,t)} \mathbf{U}^{(i_b,t)}$; // Section 3.1.3
- 4 $\mathbf{T} \leftarrow \mathbf{T} \mathbf{N}^{1DT}$; // Eq. (18)
 $\quad (bn_p^2 \times n_q) \quad (bn_p^2 \times n_p)(n_p \times n_q)$
- 5 **for** $q \leftarrow 1$ **to** n_q **do**
- 6 $\mathbf{T}_q \leftarrow \mathbf{T}_q \mathbf{N}^{1DT}$; // Eq. (19)
 $\quad (bn_p \times n_q) \quad (bn_p \times n_p)(n_p \times n_q)$
- 7 **for** $q \leftarrow 1$ **to** n_q^2 **do**
- 8 $\mathbf{T}_q \leftarrow \mathbf{T}_q \mathbf{N}^{1DT}$; // Eq. (20)
 $\quad (b \times n_q) \quad (b \times n_p)(n_p \times n_q)$
- 9 $\mathbf{T}^{(2)} \leftarrow \mathbf{T} \tilde{\mathbf{D}}^{1DT}$; // Eq. (18)
 $\quad (bn_q^2 \times n_q) \quad (bn_q^2 \times n_q)(n_q \times n_q)$
- 10 **for** $q \leftarrow 1$ **to** n_q **do**
- 11 $\mathbf{T}_q^{(1)} \leftarrow \mathbf{T}_q \tilde{\mathbf{D}}^{1DT}$; // Eq. (19)
 $\quad (bn_q \times n_q) \quad (bn_q \times n_q)(n_q \times n_q)$
- 12 **for** $q := 1$ **to** n_q^2 **do**
- 13 $\mathbf{T}_q^{(0)} \leftarrow \mathbf{T}_q \tilde{\mathbf{D}}^{1DT}$; // Eq. (20)
 $\quad (b \times n_q) \quad (b \times n_q)(n_q \times n_q)$
- 14 $[\mathbf{T}^{(0)} \ \mathbf{T}^{(1)} \ \mathbf{T}^{(2)}] \leftarrow$
 $\quad (bn_q^3 \times 3)$
 $\quad [\mathbf{T}^{(0)} \ \mathbf{T}^{(1)} \ \mathbf{T}^{(2)}] (\mathbf{J}^{(e)-1} \mathbf{J}^{(e)-T} \det \mathbf{J}^{(e)} \mu)$; // Eq. (22)
 $\quad (bn_q^3 \times 3) \quad (3 \times 3)$
- 15 $\mathbf{T} \leftarrow (\det \mathbf{J}^{(e)} \kappa) \circ \mathbf{T}$; // Eq. (21)
 $\quad (bn_q^3) \quad (n_q^3) \quad (bn_q^3)$
- 16 $\mathbf{T} \leftarrow \mathbf{T} + \mathbf{T}^{(2)} \tilde{\mathbf{D}}^{1D}$; // Eq. (18)
 $\quad (bn_q^2 \times n_q) \quad (bn_q^2 \times n_q)(bn_q^2 \times n_q)(n_q \times n_q)$
- 17 **for** $q \leftarrow 1$ **to** n_q **do**
- 18 $\mathbf{T}_q \leftarrow \mathbf{T}_q + \mathbf{T}_q^{(1)} \tilde{\mathbf{D}}^{1D}$; // Eq. (19)
 $\quad (bn_q \times n_q) \quad (bn_q \times n_q)(bn_q \times n_q)(n_q \times n_q)$
- 19 **for** $q \leftarrow 1$ **to** n_q^2 **do**
- 20 $\mathbf{T}_q \leftarrow \mathbf{T}_q + \mathbf{T}_q^{(0)} \tilde{\mathbf{D}}^{1D}$; // Eq. (20)
 $\quad (b \times n_q) \quad (b \times n_q)(b \times n_q)(n_q \times n_q)$
- 21 $\mathbf{T} \leftarrow \mathbf{T} \mathbf{N}^{1D}$; // Eq. (18)
 $\quad (bn_q^2 \times n_p) \quad (bn_q^2 \times n_q)(n_q \times n_p)$
- 22 **for** $p \leftarrow 1$ **to** n_p **do**
- 23 $\mathbf{T}_p \leftarrow \mathbf{T}_p \mathbf{N}^{1D}$; // Eq. (19)
 $\quad (bn_q \times n_p) \quad (bn_q \times n_q)(n_q \times n_p)$
- 24 **for** $p \leftarrow 1$ **to** n_p^2 **do**
- 25 $\mathbf{T}_p \leftarrow \mathbf{T}_p \mathbf{N}^{1D}$; // Eq. (20)
 $\quad (b \times n_p) \quad (b \times n_q)(n_q \times n_p)$
- 26 $\mathbf{V}^{(i_b,t)} \leftarrow \mathbf{V}^{(i_b,t)} + \mathbf{Q}^{(i_b,e,t)T} \mathbf{T}$; // Section 3.1.3
- 27 $\mathbf{V}^{(i_b,t)} \leftarrow \mathbf{C}^{(i_b,t)T} \mathbf{V}^{(i_b,t)}$; // Section 3.1.2
- 28 **return** \mathbf{V}

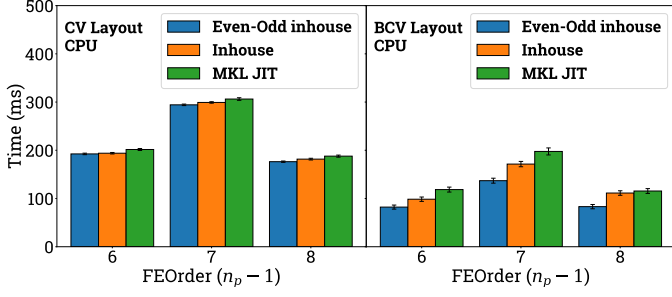


Figure 2: Benchmarking the proposed BCV layout and other implementation strategies on single core of Intel® Xeon® Gold 6248R processor. Benchmark case studies: 15625 DoFs ($n_q = n_p = 7, 9$); 24389 DoFs ($n_q = n_p = 8$).

```

1 template <int m, int n, int k>
2 inline void
3 matmul(const __m512d *A,
4         const __m512d *B,
5         __m512d *C){
6 /*Here m = n_p^2, n = n_q, k = n_p */
7 /*and A ← U^{(i_b, e, t)}, B ← [N^E N^O], C ← U^{(i_b, e, t)} N^{1D T} */
8 constexpr int ko = k / 2;
9 constexpr int no = n / 2;
10 for (auto i = 0; i < m; ++i){
11 /*Temporary arrays for storage of even and
12 odd components of rows of A*/
13 __m512d tempAe[ko], tempAo[ko];
14 /*Evaluate even and odd components of row i (
15 = p_1 + n_p p_2) of A*/
16 for (auto q = 0; q < ko; ++q){
17 /* tempAe[q] = U_{p_1, p_2, q}^{(i_b, e, t)} + U_{p_1, p_2, k-q}^{(i_b, e, t)} */
18 /* tempAo[q] = U_{p_1, p_2, q}^{(i_b, e, t)} - U_{p_1, p_2, k-q}^{(i_b, e, t)} */
19 tempAe[q] = A[i + q * m] +
20 A[i + (k - 1 - q) * m];
21 tempAo[q] = A[i + q * m] -
22 A[i + (k - 1 - q) * m];}
23 for (auto j = 0; j < no; ++j){
24 /*Temporary storage even and odd components
25 of C*/
26 __m512d tempCe, tempCo;
27 /*tempCe = ∑_q^{n_p/2} tempAe[q] N_{j,q}^E */
28 /*tempCo = ∑_q^{n_p/2} tempAo[q] N_{j,q}^O */
29 tempCe = tempAe[0] * B[j];
30 for (auto q = 1; q < ko; ++q)
31 tempCe += tempAe[q] * B[j + q * no];
32 /*tempCo = ∑_q^{n_p/2} tempAo[q] N_{j,q}^O */
33 tempCo = tempAo[0] * B[j + ko * no];
34 for (auto q = 1; q < ko; ++q)
35 tempCo += tempAo[q] * B[j + q * no + ko *
36 no];
37 /*Recombining tempCe and tempCo to get
38 elements of C */
39 /*T_{p_1, p_2, j} = tempCe + tempCo */
40 /*T_{p_1, p_2, n-j} = tempCe - tempCo*/
41 C[i + m * j] = tempCe + tempCo;
42 C[i + m * (n - 1 - j)] = tempCo - tempCe;}}

```

Listing 2: Code snippet for the evaluation of $(\mathbf{N}^{1D} \otimes \mathbf{I} \otimes \mathbf{I} \otimes \mathbf{I}) \mathbf{U}^{(i_b, e, t)}$ using the even-odd decomposition strategy. Note that this snippet is purely to illustrate the implementation strategy, and as such k and n are assumed to be even. The actual implementation is generic. Note that if $n = k$, then $C = A$ is allowed, which results in a lower memory footprint.

GPU Implementation: Evaluation of $\mathbf{A}^{(e)} \mathbf{U}^{(i_b, e, t)}$

The implementation strategy, including extraction, and assembly, used for the evaluation of $\mathbf{V}^{(t)}$ on GPU architectures is enunciated in Algorithm 4.

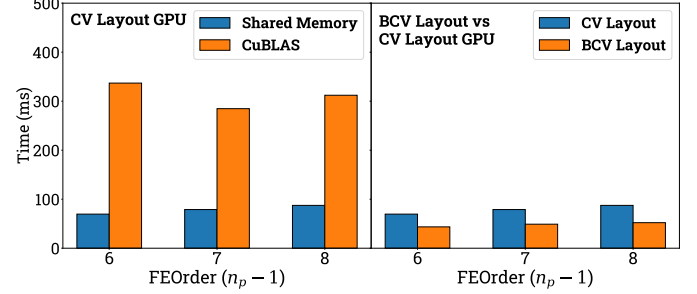


Figure 4: Benchmarking the proposed BCV layout and cuBLAS dgemm implementation of matrix-free on NVIDIA® Tesla® V100 SXM2 32GB. GPU benchmark case studies: 389017 DoFs (FEOrder=6, 8); 357911 DoFs (FEOrder=7).

For the evaluation of tensor contractions in Eqs. (18) to (20), we note that cuBLAS dgemm modules would need multiple reads from and writes to the device memory. Hence, to avoid such data movement, we design a hand-written shared memory implementation which performs better than cuBLAS dgemm modules (Fig. 4). The shared memory implementation takes advantage of kernel fusion, combining the extraction, tensor contractions, and assembly steps in one kernel to access data once from device memory and perform computations inside the fast shared memory. This reduces excess data movement from device memory.

Unlike the FE-cell level local dense matrices approach in Section 2.2.1, the shared memory kernel does not explicitly construct the cell level multi-vectors $\mathbf{U}^{(e, t)}$ and $\mathbf{V}^{(e, t)}$ in the device memory. This helps in reducing memory footprint even further. The kernel launch is as follows:

```

1 compute <int m, int n, int k> <<<dim3(E_t, n_b)
, dim3(n_tx, n_ty)>>> (double *C, const
double *A, const double *B, ...)

```

Listing 3: Kernel launch for shared memory implementation

The kernel is launched with a 2-D grid of $E_t \times n_b$ thread blocks, each with a 2-D block of $n_{t_x} = b$ threads in the x -direction and $n_{t_y} = \text{warpSize} \times \alpha$ threads in the y -direction where $\text{warpSize} = 32$ for NVIDIA GPUs and α is a tunable parameter. This choice of n_{t_y} ensures that the total number of threads per thread block is a multiple of warpSize . The values of n_{t_x} and n_{t_y} for each FEOrder are explained in Section 4.

We read the matrices \mathbf{N}^{1D} and $\tilde{\mathbf{D}}^{1D}$ into shared memory once and reuse them for all the subsequent tensor contractions. We rewrite these tensor contractions as batched-matrix-matrix multiplications as discussed in Section 3.1.4 and execute them as linear combinations of columns of \mathbf{N}^{1D} and $\tilde{\mathbf{D}}^{1D}$ (Fig. 5). Thus, evaluations like Eq. (18) can be written as

$$T_{t_x, t_y, q} = \sum_{k=1}^{n_p} R_{t_x, t_y, k} N_{qk}^{1D} \quad \forall q = 1, \dots, n_p \quad (23)$$

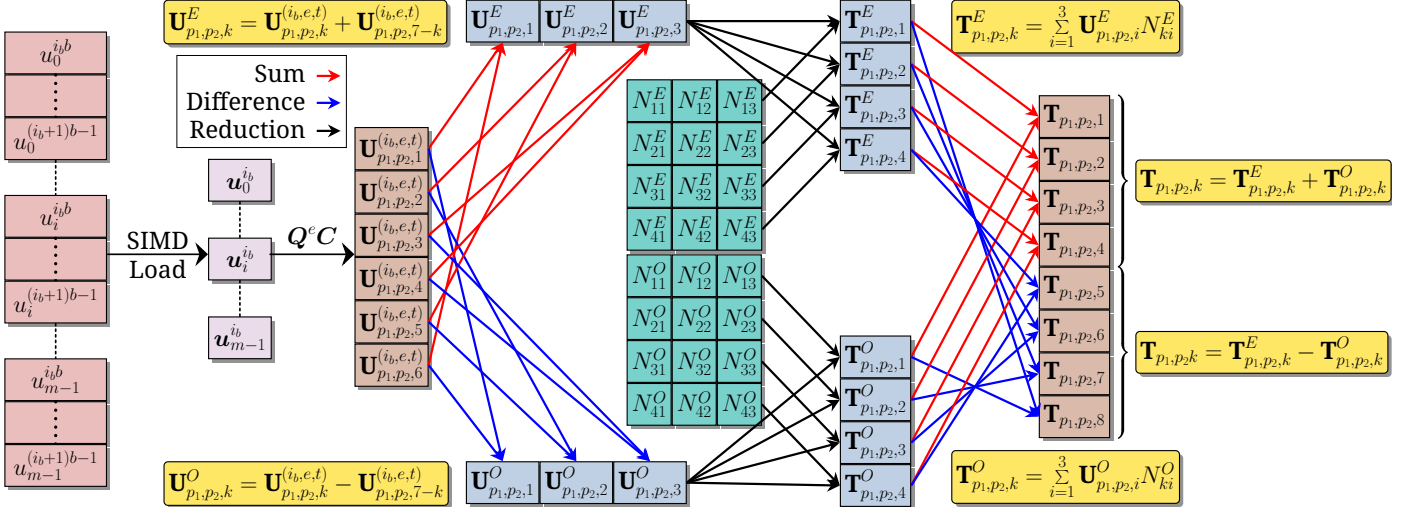


Figure 3: Evaluation of $(\mathbf{I} \otimes \mathbf{I} \otimes \mathbf{I} \otimes \mathbf{N}^{1D}) \mathbf{U}^{(ib,e)}$ using the even-odd decomposition strategy as an example with $n_p = 6$ and $n_q = 8$. Each block in \mathbf{U} represents an n_p^2 sized array of AVX-512 doubles, which are decomposed into even and odd components to be multiplied by the corresponding shape function matrices. The results are combined to form \mathbf{T} .

where t_x is `threadIdx.x` and t_y is `threadIdx.y`. This method of execution enables us to combine the extraction step and the first tensor contraction step. Thus the floating point operations can be started as soon as a portion of $\mathbf{U}^{(t)}$ is read from the device memory, without needing to wait for its complete bn_p^3 data inside shared memory. Furthermore, as each thread accesses the same values from \mathbf{N}^{1D} and $\tilde{\mathbf{D}}^{1D}$, the accesses get broadcasted, which helps reduce bank conflicts in shared memory. To further improve performance, we utilize registers to keep the data local to each thread as much as possible. This optimization reduces data movement from shared memory and better utilizes the hardware. Finally, in the assembly step `atomicAdd` is used to avoid race conditions and safely assemble the output $\mathbf{V}^{(t)}$, and similar to the extraction step, we also combine the assembly step with the last tensor contraction.

Algorithm 4: Batchwise evaluation of \mathbf{V} on GPUs

Input: \mathbf{U}

Data: $\mathbf{C}^{(t)}$, $\mathbf{B}^{(ib,t)}$, $\mathbf{Q}^{(ib,e,t)}$, \mathbf{N}^{1D} , \mathbf{D}^{1D} , \mathbf{J}^e , κ

Temporary Variables: \mathbf{T} , $\mathbf{T}^{(0)}$, $\mathbf{T}^{(1)}$, $\mathbf{T}^{(2)}$

Result: \mathbf{V}

MPI rank: t

blockIdx.x: e

blockIdx.y: i_b

- 1 $\mathbf{U}^{(t)} \leftarrow \mathbf{C}^{(t)} \mathbf{U}^{(t)}$; // Section 3.1.2
- /* Device kernel compute starts */
- 2 $\mathbf{T} \leftarrow \mathbf{Q}^{(ib,e,t)} \mathbf{B}^{(ib,t)} \mathbf{U}^{(t)} \mathbf{N}^{1DT}$; // Sections 3.1.1 and 3.1.3 and Eq. (18)
 $(bn_p^2 \times n_q) \quad (bn_p^2 \times n_p) \quad (n_p \times n_q)$
- 3 $\mathbf{T}_q^{(0)} \leftarrow \mathbf{T}_q \mathbf{N}^{1DT} \quad \forall q = 1, \dots, n_q$; // Eq. (19)
 $(bn_p \times n_q) \quad (bn_p \times n_p)(n_p \times n_q)$
- 4 $\mathbf{T}_q \leftarrow \mathbf{T}_q^{(0)} \mathbf{N}^{1DT} \quad \forall q = 1, \dots, n_q^2$; // Eq. (20)
 $(b \times n_q) \quad (b \times n_p)(n_p \times n_q)$
- 5 $\mathbf{T}^{(2)} \leftarrow \mathbf{T} \tilde{\mathbf{D}}^{1DT}$; // Eq. (18)
 $(bn_q^2 \times n_q) \quad (bn_q^2 \times n_q)(n_q \times n_q)$
- 6 $\mathbf{T}_q^{(1)} \leftarrow \mathbf{T}_q \tilde{\mathbf{D}}^{1DT} \quad \forall q = 1, \dots, n_q$; // Eq. (19)
 $(bn_q \times n_q) \quad (bn_q \times n_q)(n_q \times n_q)$
- 7 $\mathbf{T}_q^{(0)} \leftarrow \mathbf{T}_q \tilde{\mathbf{D}}^{1DT} \quad \forall q = 1, \dots, n_q^2$; // Eq. (20)
 $(b \times n_q) \quad (b \times n_q)(n_q \times n_q)$
- 8 $[\mathbf{T}^{(0)} \mathbf{T}^{(1)} \mathbf{T}^{(2)}] \leftarrow [\mathbf{T}^{(0)} \mathbf{T}^{(1)} \mathbf{T}^{(2)}] (\mathbf{J}^{(e-1)} \mathbf{J}^{(e)-T} \det \mathbf{J}^{(e)} \mu)$; // Eq. (18)
 $(bn_q^3 \times 3) \quad (bn_q^3 \times 3) \quad (3 \times 3)$
- 9 $\mathbf{T} \leftarrow (\det \mathbf{J}^{(e)} \kappa) \circ \mathbf{T} + \mathbf{T}^{(2)} \tilde{\mathbf{D}}^{1D}$; // Eq. (18)
 $(bn_q^2 \times n_q) \quad (n_q^3) \quad (bn_q^3) \quad (bn_q^2 \times n_q)(n_q \times n_q)$
- 10 $\mathbf{T}_q \leftarrow \mathbf{T}_q + \mathbf{T}_q^{(1)} \tilde{\mathbf{D}}^{1D} \quad \forall q = 1, \dots, n_q$; // Eq. (19)
 $(bn_q \times n_q) \quad (bn_q \times n_q) \quad (bn_q \times n_q)(n_q \times n_q)$
- 11 $\mathbf{T}_q \leftarrow \mathbf{T}_q + \mathbf{T}_q^{(0)} \tilde{\mathbf{D}}^{1D} \quad \forall q = 1, \dots, n_q^2$; // Eq. (20)
 $(b \times n_q) \quad (b \times n_q) \quad (b \times n_q)(n_q \times n_q)$
- 12 $\mathbf{T} \leftarrow \mathbf{T} \mathbf{N}^{1D}$; // Eq. (18)
 $(bn_q^2 \times n_q) \quad (bn_q^2 \times n_q)(n_q \times n_q)$

```

1 /* Snippet for Eq. (20) */
2 /*  $m = n_p^2$ ,  $n = n_q$ ,  $k = n_p$  */
3 /*  $A \leftarrow R$ ,  $B \leftarrow N^{1D^T}$ ,  $C \leftarrow T = RN^{1D^T}$  */
4 for (int i = threadIdx.y; i < m; i += blockDim.y)
5 {
6     /* Temporary arrays for storage of rows of A
7     and C */
8     double y[n], x[k];
9     for (int j = 0; j < n; j++)
10         y[j] = 0.0;
11     /*  $x[q] = R_{ix,iq}$  */
12     for (int q = 0; q < k; q++) {
13         x[q] = A[threadIdx.x + i * b + q * b * m];
14         /*  $y[j] = \sum_q R_{ix,iq} N_{jq}$  */
15         for (int j = 0; j < n; j++)
16             y[j] += B[j + q * n] * x[q];
17     }
18     /*  $T_{ix,ij} = y[j]$  */
19     for (int j = 0; j < n; j++)
20         C[threadIdx.x + i * b + j * b * m] = y[j];
21 }
22 /* Snippet for Eq. (19) */
23 /*  $m = n_p^2$ ,  $n = n_q$ ,  $k = n_p$  */
24 /*  $A \leftarrow R_v$ ,  $B \leftarrow N^{1D^T}$ ,  $C \leftarrow T_v = R_v N^{1D^T} \quad \forall v = 1, \dots, n_p$  */
25 for (int i = threadIdx.y; i < m; i += blockDim.y)
26 {
27     /* Temporary arrays for storage of rows of A
28     and C */
29     double y[n], x[k];
30     int u = i % k, v = i / k;
31     for (int j = 0; j < n; j++)
32         y[j] = 0.0;
33     /*  $x[q] = R_{ix,u,q,v}$  */
34     for (int q = 0; q < k; q++) {
35         x[q] = A[threadIdx.x + u * b + q * b * k + v
36             * b * k^2];
37         /*  $y[j] = \sum_q R_{ix,u,q,v} N_{jq}$  */
38         for (int j = 0; j < n; j++)
39             y[j] += B[j + q * n] * x[q];
40     }
41     /*  $T_{ix,u,j,v} = y[j]$  */
42     for (int j = 0; j < n; j++)
43         C[threadIdx.x + u * b + j * b * k + v * b * k
44             * n] = y[j];
45 }
46 /* Snippet for Eq. (18) */
47 /*  $m = n_q^2$ ,  $n = n_q$ ,  $k = n_p$  */
48 /*  $A \leftarrow R_v$ ,  $B \leftarrow N^{1D^T}$ ,  $C \leftarrow T_v = R_v N^{1D^T} \quad \forall v = 1, \dots, n_p^2$  */
49 for (int i = threadIdx.y; i < m; i += blockDim.y)
50 {
51     /* Temporary arrays for storage of rows of A
52     and C */
53     double y[n], x[k];
54     for (int j = 0; j < n; j++)
55         y[j] = 0.0;
56     /*  $x[q] = R_{ix,q,i}$  */
57     for (int q = 0; q < k; q++) {
58         x[q] = A[threadIdx.x + q * b + i * b * k];
59         /*  $y[j] = \sum_q R_{ix,q,i} N_{jq}$  */
60         for (int j = 0; j < n; j++)
61             y[j] += B[j + q * n] * x[q];
62     }
63     /*  $T_{ix,ji} = y[j]$  */
64     for (int j = 0; j < n; j++)
65         C[threadIdx.x + j * b + i * b * n] = y[j];
66 }

```

Listing 4: Code snippets for the evaluation of equation 18, 19 and 20 on GPUs. Note that this snippet is purely to illustrate the implementation strategy and the actual implementation is generic.

Algorithm 5: Overlap of computation and communication

```

Input:  $U$ 
Data:  $B^{(i_b)}, P^{(i_b,t)}, C^{(i_b,t)}, Q^{(i_b,e,t)}$  for  $e = 1, \dots, E_t$  and
 $i_b = 1, \dots, n_b$ 
Result:  $V$ 
MPI rank:  $t$ 
1  $U^{t,1} \leftarrow P^{t,1} B^1 U$ ;
2 for  $i_b \leftarrow 1$  to  $n_b$  do
    /* Start communication for batch  $i_b + 1$ 
    required for the evaluation of
 $P^{t,i_b+1} B^{(i_b+1)} U$  using MPI_Isend and MPI_Irecv
    */
3     if  $i_b < n_b$  then
4         Start :  $U^{t,i_b+1} \leftarrow P^{t,i_b+1} B^{(i_b+1)} U$ ;
    /* Start communication for batch  $i_b - 1$ 
    required for the evaluation of
 $P^{t,i_b-1} B^{(i_b-1)T} V^{t,i_b-1}$  using MPI_Isend and
    MPI_Irecv. */
5     if  $i_b > 1$  then
6         Start :  $V \leftarrow V + P^{t,i_b-1} B^{(i_b-1)T} V^{t,i_b-1}$ ;
    /* Using Algorithm 3 for the following
    evaluation. */
7      $V^{(i_b,t)} \leftarrow C^{(i_b,t)T} \left( \sum_e Q^{e,i_b,t} A^{(e)} Q^{e,i_b,t} \right) C^{(i_b,t)} U^{(i_b,t)}$ ;
    /* MPI_Waitall for finishing communication
    and processing the recieved data. */
8     if  $i_b < n_b$  then
9         Finish :  $U^{t,i_b+1} \leftarrow P^{t,i_b+1} B^{(i_b+1)} U$ ;
10    if  $i_b > 1$  then
11        Finish :  $V \leftarrow V + P^{t,i_b-1} B^{(i_b-1)T} V^{t,i_b-1}$ ;
12  $V^{t,n_b} \leftarrow P^{t,n_b} B^{n_b} V^{t,n_b}$ ;
13 return  $V$ 

```

3.1.5. Distributed Parallelism: MPI aspects

We exploit distributed parallelism over the subdomain partitioning. Each MPI task with rank t owns a subdomain t with FE-cells $1, 2, \dots, E_t$ such that $\sum_t E_t = E$.

CPU Implementation: MPI aspects

It is important to note that in our implementation, we do not explicitly construct $B^{(i_b)} U$ in memory. Instead, we evaluate the action of $P^{(i_b,t)}$ on it through MPI communication of boundary data for the multi-vectors across tasks that share subdomain boundaries. Additionally, we evaluate the summations over e and i_b in Eq. (14) as serial loops. Furthermore, we overlap the communication involved in the action of $P^{(i_b,t)} B^{(i_b)}$ and $B^{(i_b)T} P^{(i_b,t)T}$ with the computation involved in the action of $C^{(i_b)}$, $C^{(i_b)T}$, $Q^{(e,i_b)}$, $Q^{(e,i_b)T}$ and $A^{(e)}$ as illustrated in Algorithm 5

GPU Implementation: MPI aspects

On GPUs, we do not explicitly construct U in device memory. Instead, we evaluate the action of $P^{(t)}$ on U by MPI communication of boundary data for the multi-vectors across tasks that share subdomain boundaries. We apply $C^{(t)}$ and then evaluate

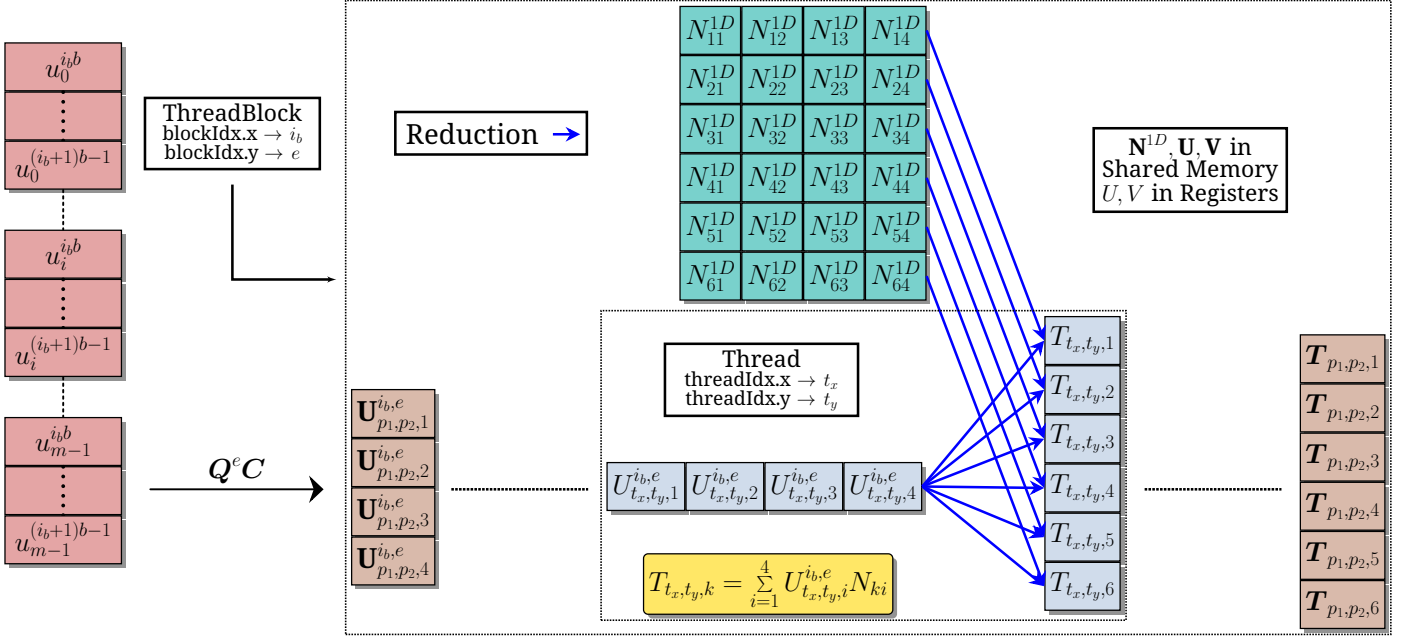


Figure 5: Pictorial depiction of tensor contractions done on GPUs. The extraction and first tensor contraction steps of evaluation of $\mathbf{A}^{(e)} \mathbf{U}^{(i_b, e, t)}$ are depicted for the case of $n_p = 4$ and $n_q = 8$. Each block in \mathbf{U} represents n_p^2 sized array of b doubles.

the summations over e and i_b in Eq. (15) by launching a single kernel of a 2-D grid consisting of $E_t \times n_b$ thread blocks as illustrated in Algorithm 5. Finally we apply $\mathbf{C}^{(t)T}$ and then $\mathbf{P}^{(t)T}$.

4. Performance Benchmarks

The benchmark problem we consider is the Helmholtz problem obtained by setting $\mu = 1$ and $\kappa(\mathbf{x}) = 2\pi \forall \mathbf{x} \in \Omega$ in Eq. (1). For this purpose, we selected the number of nodes for the 1D base mesh to be $n_p = 7, 8, 9$, resulting in Lagrange interpolating polynomial orders FEOrder = 6, 7, 8. Furthermore, we use a quadrature rule of the order, $n_q = n_p$, to perform the integrals involved. We benchmark the performance of our implementation for this problem on two computing clusters whose configurations we describe in Table 1.

System Config	Local Cluster	Param Pravega (CPU only nodes)
Processor	Intel® Xeon® Gold 6248R	Intel® Xeon® Platinum 8268
GPU	NVIDIA® Tesla® V100 SXM2 32GB	-
Nodes	2	428+156(High Memory)
CPU cores/Node	48	48
GPUs/Node	8	-
Memory/Node	512 GB DDR4 + 256 GB HBM2	192 GB or 768 GB (High Memory), DDR4
Peak Performance	124.8 TF (V100 DP)	1.459 TF (AVX-512 DP)
Interconnect	Mellanox® ConnectX®-5 MT27800	Mellanox® ConnectX®-6 MT28908

Table 1: System configurations for the benchmark architectures.

The FE mesh considered is uniform, and the boundary conditions chosen are the homogeneous Dirichlet boundary conditions. We use deal.II library version 9.4.0 [27] with the p4est[28] backend to perform the MPI-parallel meshing and domain decomposition.

4.1. CPU Benchmarks

In our study, we employed the use of Intel® legacy compilers (icc/icpc) version 2021.7.0 in conjunction with the Intel® oneAPI MPI version 2021.5.0. We utilized the optimization flags `-O3 -qopenmp-simd -march=native` in order to leverage architecture-specific compiler optimizations. Furthermore, we utilized the BLAS implementations from Intel® oneAPI MKL version 2022.0.1. Additionally, we employed the marker

API of the LIKWID tool [29] with the `perf_event` backend to obtain performance metrics on CPU architectures. To this end, we executed the MPI executable using the command :

```
1 likwid-mpirun -np $NTASKS -g MEM_DP -m \
   $EXECUTABLE
```

Listing 5: MPI execution call

In Fig. 6, we show the sustained performance and strong scaling efficiencies of our implementation for FEOrder= 6, 7, 8 and $n_v = 8, 16, 32, 64, 128, 256, 512, 1024$ until 1536 MPI tasks. This scaling study ranges from $\sim 13k$ DoFs per processor to ~ 400 DoFs per processor in the case of FEOrder= 6, 7 and $\sim 14.5k$ DoFs per processor to ~ 450 DoFs per processor in the case of FEOrder= 8. We note that even in the extreme scaling regime of a few hundred DoFs per processor, our implementation maintains strong scaling efficiencies of 40 – 60%. The highest sustained performance achieved is 11.72 TFLOPS/s, which is 25% of the theoretical peak performance. We note that the matrix-free approach reduces the arithmetic complexity at the cost of increased data movement and, as such, struggles to reach a higher percentage of the theoretical peak performance.

We also benchmark our implementation against the baselines of the cell-matrix and `deal.II` matrix-free implementation. As demonstrated by Das et al. [3, 21] and verified by us, the CV layout is superior to the BCV layout in the case of cell-matrix, and as such, we use the CV layout for the cell-matrix implementation. We also implement the constraints and extraction/assembly operations in the same fashion as we do for the matrix-free implementation (discussed in Sections 3.1.2 and 3.1.3). We evaluate the cell-level products $\mathbf{V}^{(e,t)} = \mathbf{A}^{(e)} \mathbf{U}^{(e,t)}$ using the `dgemm_batch_strided` module from Intel® oneAPI MKL version 2022.0.1 which was found to be superior or comparable to the JIT based implementation. For the case of the `deal.II` matrix-free implementation, we find that the provided multi-component vector implementation was not very efficient when the number of components was in the hundreds. Instead, we implement the FE-discretized matrix multi-vector product using the `deal.II`'s single-component matrix-free implementa-

tion by looping over the constituent vectors, which is equivalent to setting $n_b = n_v$ in our framework. Note that `deal.II` also utilizes SIMD vectorization, but unlike our approach, they treat multiple FE-cells concurrently using hardware intrinsics.

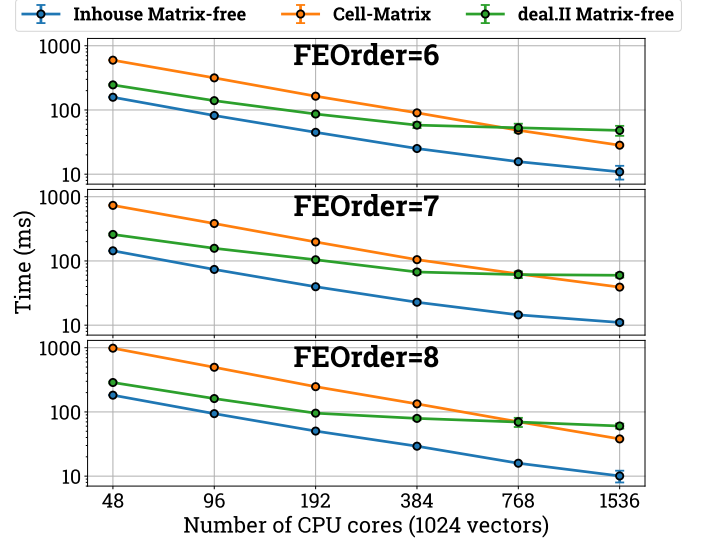


Figure 7: Comparative scaling study of our implementation with respect to the cell-matrix method and `deal.II` matrix-free implementation for $n_v = 1024$. Case studies: 614125 DoFs (FEOrder=6, 7); 704969 DoFs (FEOrder=8).

In Fig. 7, we show the scaling data of our implementation compared to the cell-matrix and the `deal.II` matrix-free implementations. We note that our implementation has a clear and noticeable performance advantage over the cell-matrix and the `deal.II` matrix-free implementations across varying MPI tasks. The quantitative performance advantage over both the baseline implementations varies with MPI tasks. As such, we show the comparisons in more detail (with varying n_v) for 48 and 1536 MPI tasks in Figs. 8 and 9 respectively.

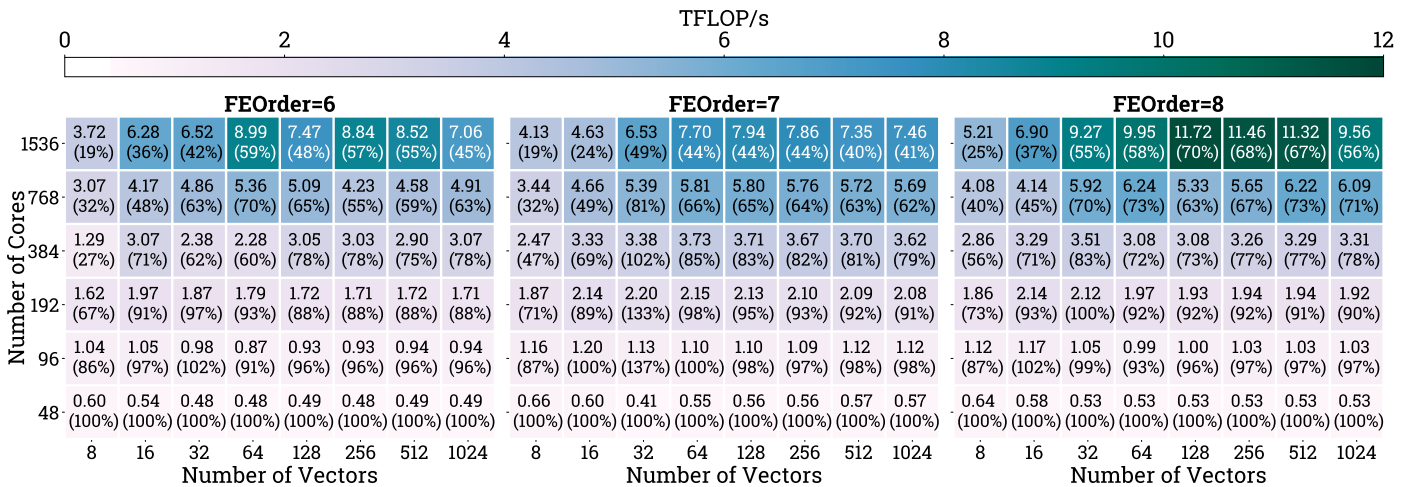


Figure 6: Scaling study of our implementation. Case studies: 614125 DoFs (FEOrder=6, 7); 704969 DoFs (FEOrder=8).

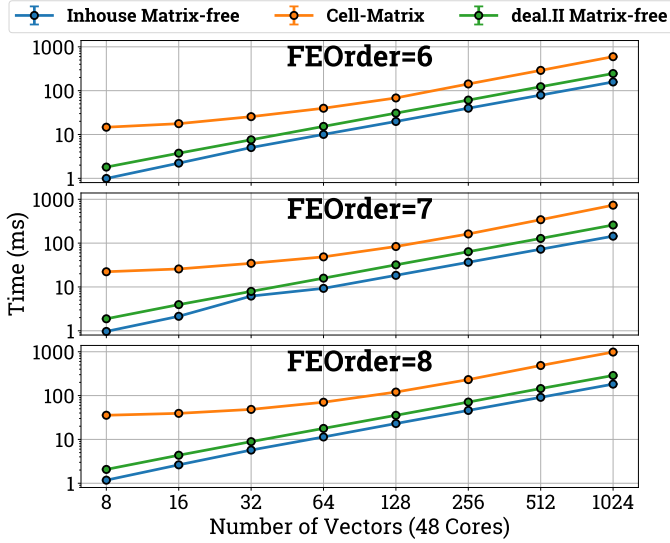


Figure 8: Performance benchmark of our implementation against the cell-matrix and deal.II matrix-free baseline implementations on 48 MPI tasks. Case studies: 614125 DoFs (FEOrder=6, 7); 704969 DoFs (FEOrder=8).

From Fig. 8, we see that the closest competitor to our implementation at every value of n_v in the regime of $\sim 13k - 14k$ DoFs per core is the deal.II matrix-free implementation. We note that our implementation shows a performance improvement ranging from 1.28x to 1.94x over the deal.II matrix-free implementation in this scaling regime.

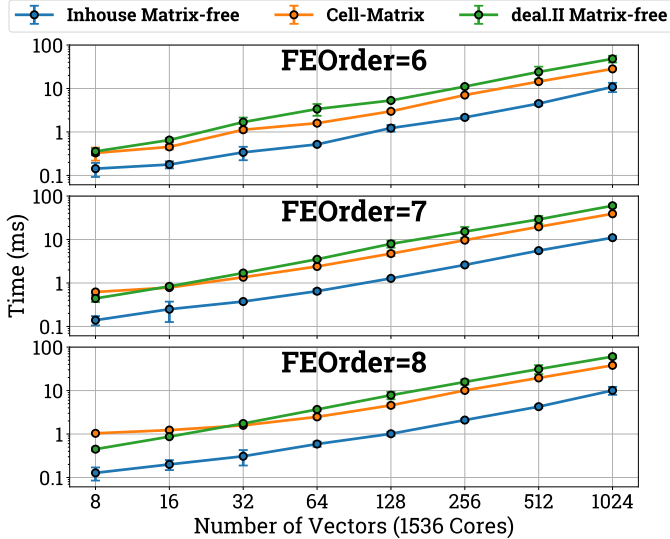


Figure 9: Performance benchmark of our implementation against the cell-matrix and deal.II matrix-free baseline implementations on 1536 MPI tasks. Case studies: 614125 DoFs (FEOrder=6, 7); 704969 DoFs (FEOrder=8).

On the other extreme, from Fig. 9, we see that the closest competitor to our implementation at most values of n_v in the regime of $\sim 400 - 450$ DoFs per core is the cell-matrix implementation. For some values of $n_v < 16$, the deal.II matrix-free implementation is still superior to the cell-matrix implementation. We attribute the poor scaling of the deal.II matrix-free implementation to the utilization of SIMD vectorization for

FE-cells becomes inefficient in this regime as there are fewer FE-cells per MPI task. On the other hand, our implementation does not have this drawback. We note that our implementation shows a performance improvement ranging from 2.30x to 5.13x over the closest baseline implementation in this scaling regime.

4.2. GPU Benchmarks

The performance metrics are collected on NVIDIA® Tesla® V100 SXM2 32GB and the code was compiled using GCC 11.3, CUDA NVCC 11.7 and OpenMPI 4.1.3. The flag used for compilation is `-arch=sm_70` which is necessary to use `atomicAdd` function inside compute kernel for matrix-free approach. In case of cell-matrix approach, `-lcublas` flag is passed to the compiler for using `cublasDgemmStridedBatched` module from CUDA 11.7.

The times were collected through `clock_gettime` function with `CLOCK_MONOTONIC` argument as it has nanosecond resolution and appropriate barriers `MPI_Barrier` and `cudaDeviceSynchronize` were used around the code of interest. The timings were repeated 100 times and the mean time was taken for all performance studies. NVIDIA® Nsight™ Compute 2022.4 profiler was used to get the total floating point operations. `cudaProfilerStart` and `cudaProfilerStop` were used to mark the code of interest, and the following wrapper script is used with `mpirun` to profile:

```

1 metrics+="
2 sm__sass_thread_inst_executed_op_dadd_pred_on.sum
3 sm__sass_thread_inst_executed_op_dfma_pred_on.sum
4 sm__sass_thread_inst_executed_op_dmul_pred_on.sum
5
6 ncu --metrics $metrics --profile-from-start off
  --target-processes all $EXECUTABLE

```

Listing 6: Wrapper script for profiling with Nsight Compute for multi-node GPUs

The compute kernel (Listing 3) is launched with a 2-D grid of $E_t \times n_b$ thread blocks, each with a 2-D block of $n_{t_x} = b$ threads in the x-direction and $n_{t_y} = \text{warpSize} \times \alpha$ threads in the y-direction where `warpSize` = 32 for NVIDIA GPUs and α is a tunable parameter. The optimal values for batch size b and α are determined for each FEOrder through benchmarking for various values within limits allowed by the GPU hardware. For example, V100 GPUs have a default limit of shared memory as 48 kB, and this can be increased to a maximum of 96 kB by the user. Hence, b determines the portion of the available shared memory for the kernel to use. And the value of α is limited by both the maximum number of threads per thread block and the maximum number of registers per thread block. These in turn determine the values of n_{t_x} and n_{t_y} for the kernel launch for each FEOrder. Through sustained performance analysis we show the optimal values of n_{t_x} and n_{t_y} . For FEOrder = 6: $b = 4, \alpha = 2$, for FEOrder = 7: $b = 5, \alpha = 2$, and for FEOrder = 8: $b = 4, \alpha = 4$.

These optimal values are used to conduct subsequent benchmarking studies. For the benchmark of the Helmholtz problem, we choose a uniform FE mesh such that the number of degrees

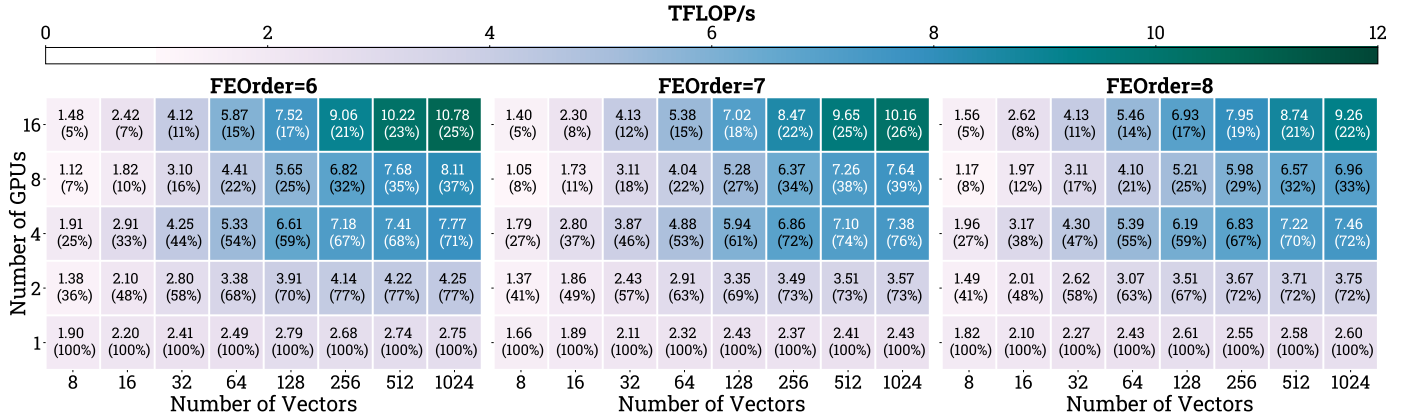


Figure 10: Scaling study of our implementation on V100 GPUs. Case studies: 389017 DoFs (FEOrder=6, 8); 357911 DoFs (FEOrder=7)

of freedom for FEOrder = 6 and 8 is 389017 and FEOrder = 7 is 357911. We then evaluate the performance of our matrix-free implementation by performing a scaling study with the number of vectors ($n_v = 8, 16, 32, 64, 128, 256, 512, 1024$) and the number of GPUs ranging from 1 to 16 (Fig. 10). This scaling study ranges from ~24k DoFs per GPU to ~390k DoFs per GPU for FEOrder = 6 and 8 and ~22k DoFs per GPU to ~360k DoFs per GPU for FEOrder = 7. We observe that for a large number of vectors like 1024, our implementation maintains an efficiency of ~71-76% for 4 GPUs and ~22-26% for 16 GPUs. For a single GPU, 1024 vectors case, matrix-free achieves ~2.75 TFLOP/s which is about 33% of the peak performance of a NVIDIA® V100 GPU.

We then compare our matrix-free implementation against the cell-matrix approach (Section 2.2.1) for multivectors, and as discussed in Section 4.1, we use CV layout for the cell-matrix implementation. We also implement the constraints and extraction/assembly operations in a similar fashion as we do for the matrix-free implementation (discussed in Sections 3.1.2 and 3.1.3). We evaluate the cell-level products $\mathbf{V}^{(e,t)} = \mathbf{A}^{(e)}\mathbf{U}^{(e,t)}$ using the cublasDgemmStridedBatched module from NVIDIA® CUDA 11.7. Currently, state-of-the-art finite-element (FE) libraries like dealii do not have a multi-vector matrix-free implementation on GPUs, and hence we compare only against the cell-matrix approach for multi-vectors.

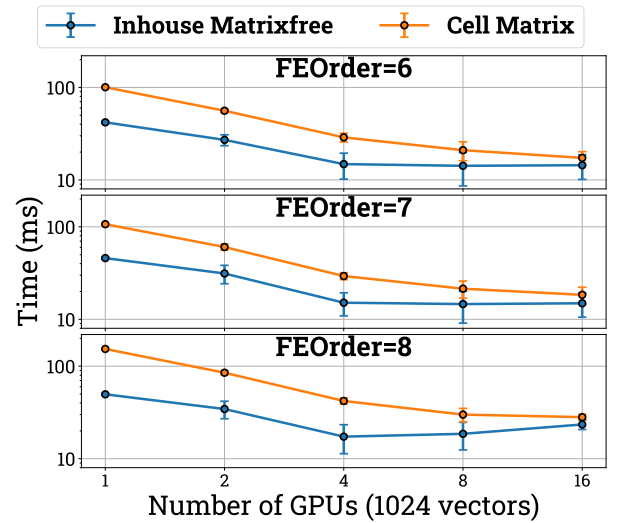


Figure 11: Comparative scaling study of our implementation concerning the cell-matrix method for $n_v = 1024$. Case studies: 389017 DoFs (FEOrder=6, 8); 357911 DoFs (FEOrder=7) for the Helmholtz problem on GPUs.

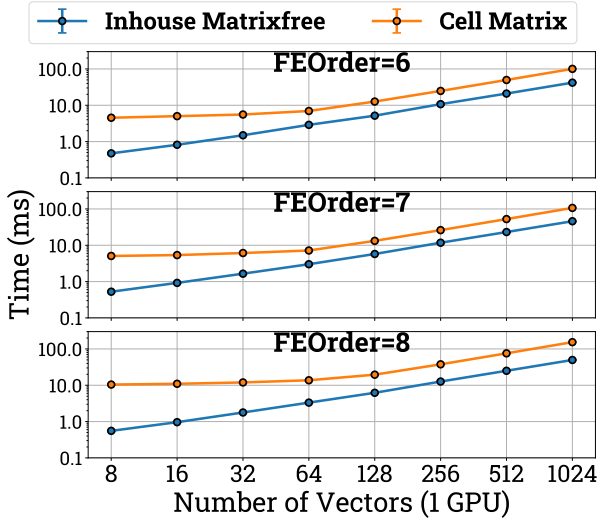


Figure 12: Performance benchmark of our implementation against the cell-matrix method on 1 GPU. Case studies: 389017 DoFs (FEOrder=6, 8); 357911 DoFs (FEOrder=7) for the Helmholtz problem on GPUs.

We perform a strong scaling study with the two approaches for 1024 vectors and $\sim 360\text{k}$ - 390k DoFs to show the performance, and Fig. 11 shows the time taken by the two approaches. Our GPU matrix-free implementation has a significant performance advantage over the cell-matrix method across all MPI tasks for FEOrder = 6, 7, and 8. As such, we show the comparisons in more detail (with varying n_v) for 1 and 8 GPUs in Figs. 12 and 13 respectively.

Performing benchmarks for various numbers of vectors on a single GPU (Fig. 12), we observe speedups of 2.4x for FEOrder = 6 and 7 and a 3.1x speedup for FEOrder = 8 over the cell-matrix method in the case of 1024 vectors. And in the case of 8 vectors, we observe speedups of 9.6x for FEOrder = 6 and 7 and an 18.8x speedup for FEOrder = 8 over the cell-matrix method.

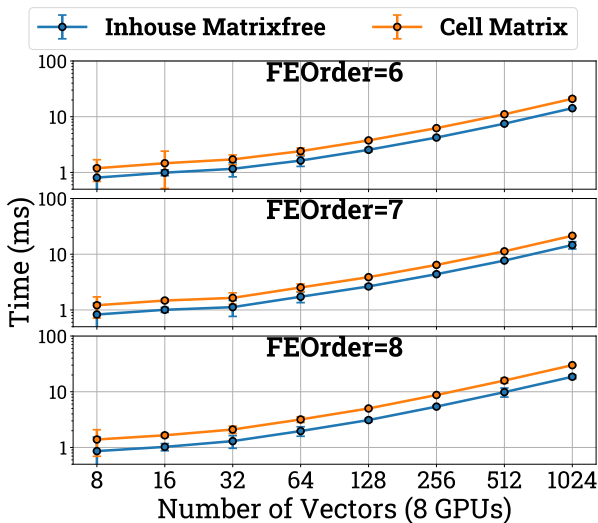


Figure 13: Performance benchmark of our implementation against the cell-matrix method on 8 GPU. Case studies: 389017 DoFs (FEOrder=6, 8); 357911 DoFs (FEOrder=7) for the Helmholtz problem on GPUs.

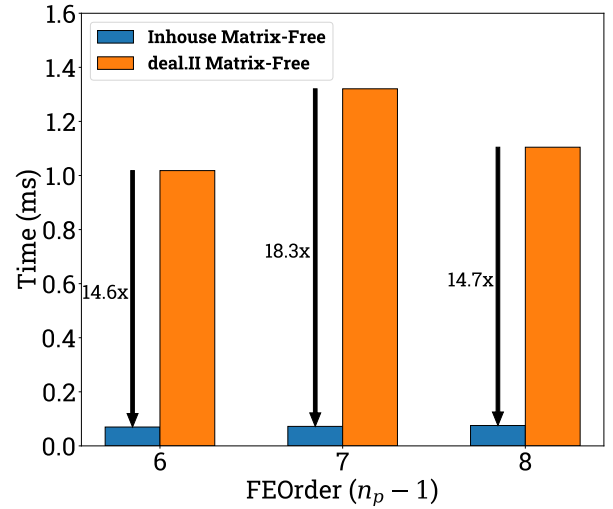


Figure 14: Performance benchmark of our implementation against the deal.II's matrix-free on 1 GPU. Case studies: 389017 DoFs (FEOrder=6, 8); 357911 DoFs (FEOrder=7) for the Helmholtz problem on GPUs.

On the other extreme of 8 GPUs, performing benchmarks for various numbers of vectors (Fig. 13), we observe speedups of 1.5x for FEOrder = 6 and 7 and 1.6x for FEOrder = 8 against the cell-matrix method for all vectors.

We also compare our GPU matrix-free to deal.II's matrix-free for a single vector on a single GPU (Fig. 14) and observe a 14.6x speedup for FEOrder = 6, 18.3x for FEOrder = 7, and a 14.7x speedup for FEOrder = 8. The same single vector comparison with the cell-matrix on a single GPU shows that our implementation has a 31.4x speedup for FEOrder 6, a 36.4x speedup for FEOrder 7, and a 54.3x speedup for FEOrder 8.

5. Conclusion and future work

In conclusion, this work presents an efficient and hardware-aware implementation procedure for the matrix-free algorithm designed to compute FE-discretized matrix-multivector products on multi-node CPU-only and multi-node GPU architectures. Our implementation employs different techniques for each architecture to achieve the best possible performance. For CPU architectures, we use even-odd decomposition to reduce computation, SIMD vectorization to exploit thread-level parallelism, and overlapping computation and communication to increase scaling efficiency. In contrast, for GPU architectures, we employ kernel fusion and GPU shared memory to reduce accesses from device memory, registers to reduce bank conflicts, and design the algorithm to overlap compute and data movement. These techniques allow us to achieve significant performance gains. Our results indicate that this implementation outperforms the closest benchmark, achieving computational gains of 3.1x on 1 GPU (390k DoFs/GPU), 1.6x on 8 GPUs (49k DoFs/GPU), and 4.4x on 768 CPU cores (~ 920 DoFs/core) for matrix-multivector products (1024 vectors) for polynomial order 8. Additionally, the strong scaling studies and performance benchmarks we show on both multi-node CPU and GPU architectures demonstrate the effectiveness of this implementation in solving large-scale problems

over the existing matrix-free implementations. This proposed method fills a gap in the current available open-source implementations of the matrix-free methods, which are neither optimal nor directly applicable for the action of an FE-discretized operator on a large number of FE-discretized fields.

In terms of future work, we believe that the proposed method will be particularly suitable for solving large-scale nonlinear eigenvalue problems arising in the quantum modeling of materials using density functional theory, as well as for solving linear systems of equations arising from FE discretizations with multiple RHS vectors. We intend to benchmark our implementation for the Chebyshev Filtered Subspace Iteration (ChFSI) [30] algorithm for solving large-scale nonlinear eigenvalue problems and the Block Conjugate Gradient (BCG) [31] algorithm for solving linear systems of equations arising from FE discretizations with multiple RHS vectors. Furthermore, we plan to explore further optimization on GPU architectures involving texture memory, constant memory, tensor cores, streams, and other GPU-specific optimizations.

References

- [1] G. F. Carey, E. Barragy, R. McLay, M. Sharma, Element-by-element vector and parallel computations, *Communications in Applied Numerical Methods* 4 (1988) 299–307. URL: <https://onlinelibrary.wiley.com/doi/10.1002/cnm.1630040303>. doi:10.1002/cnm.1630040303.
- [2] P. Motamarri, S. Das, S. Rudraraju, K. Ghosh, D. Davydov, V. Gavini, DFT-FE – A massively parallel adaptive finite-element code for large-scale density functional theory calculations, *Computer Physics Communications* 246 (2020) 106853. URL: <https://linkinghub.elsevier.com/retrieve/pii/S0010465519302309>. doi:10.1016/j.cpc.2019.07.016.
- [3] S. Das, P. Motamarri, V. Subramanian, D. M. Rogers, V. Gavini, DFT-FE 1.0: A massively parallel hybrid CPU-GPU density functional theory code using finite-element discretization, *Computer Physics Communications* 280 (2022) 108473. URL: <https://linkinghub.elsevier.com/retrieve/pii/S0010465522001928>. doi:10.1016/j.cpc.2022.108473.
- [4] K. Ljungkvist, Matrix-Free Finite-Element Computations on Graphics Processors with Adaptively Refined Unstructured Meshes, in: *Proceedings of the 25th High Performance Computing Symposium, HPC '17*, Society for Computer Simulation International, San Diego, CA, USA, 2017, pp. 1–12.
- [5] M. Kronbichler, K. Kormann, A generic interface for parallel cell-based finite element operator application, *Computers & Fluids* 63 (2012) 135–147. URL: <https://linkinghub.elsevier.com/retrieve/pii/S0045793012001429>. doi:10.1016/j.compfluid.2012.04.012.
- [6] D. Davydov, J. Pelteret, D. Arndt, M. Kronbichler, P. Steinmann, A matrix-free approach for finite-strain hyperelastic problems using geometric multigrid, *International Journal for Numerical Methods in Engineering* 121 (2020) 2874–2895. URL: <https://onlinelibrary.wiley.com/doi/10.1002/nme.6336>. doi:10.1002/nme.6336.
- [7] P. Fischer, M. Min, T. Rathnayake, S. Dutta, T. Kolev, V. Dobrev, J.-S. Camier, M. Kronbichler, T. Warburton, K. Świrydowicz, J. Brown, Scalability of high-performance PDE solvers, *The International Journal of High Performance Computing Applications* 34 (2020) 562–586. URL: <http://journals.sagepub.com/doi/10.1177/1094342020915762>. doi:10.1177/1094342020915762.
- [8] D. Arndt, W. Bangerth, D. Davydov, T. Heister, L. Heltai, M. Kronbichler, M. Maier, J.-P. Pelteret, B. Turcksin, D. Wells, *The deal.II finite element library*, 2019. URL: <https://www.dealii.org/>.
- [9] R. Anderson, J. Andrej, A. Barker, J. Bramwell, J. S. Camier, J. Cerveny, V. Dobrev, Y. Dudouit, A. Fisher, T. Kolev, W. Pazner, M. Stowell, V. Tomov, I. Akkerman, J. Dahm, D. Medina, S. Zampini, MFEM: A modular finite element methods library, *Computers & Mathematics with Applications* 81 (2021) 42–74. doi:10.1016/J.CAMWA.2020.06.009.
- [10] J. Brown, A. Abdelfattah, V. Barra, N. Beams, J.-S. Camier, V. Dobrev, Y. Dudouit, L. Ghaffari, T. Kolev, D. Medina, W. Pazner, T. Ratnayaka, J. Thompson, S. Tomov, libCEED: Fast algebra for high-order element-based discretizations, *Journal of Open Source Software* 6 (2021) 2945. doi:10.21105/joss.02945.
- [11] K. Świrydowicz, N. Chalmers, A. Karakus, T. Warburton, Acceleration of tensor-product operations for high-order finite element methods, *The International Journal of High Performance Computing Applications* 33 (2019) 735–757. URL: <http://journals.sagepub.com/doi/10.1177/1094342018816368>. doi:10.1177/1094342018816368.
- [12] T. J. R. Hughes, *The Finite Element Method: Linear Static and Dynamic Finite Element Analysis*, Dover Civil and Mechanical Engineering, Dover Publications, 2012. URL: <https://books.google.co.in/books?id=cHH2n-qBK0IC>.
- [13] J. Sun, A. Zhou, *Finite Element Methods for Eigenvalue Problems*, Chapman and Hall/CRC, 2016. URL: <https://www.taylorfrancis.com/books/9781482254655>. doi:10.1201/9781315372419.
- [14] E. Tsuchida, M. Tsukada, Adaptive finite-element method for electronic-structure calculations, *Physical Review B - Condensed Matter and Materials Physics* 54 (1996) 7602–7605. doi:10.1103/PhysRevB.54.7602.
- [15] K. Ghosh, H. Ma, V. Gavini, G. Galli, All-electron density functional calculations for electron and nuclear spin interactions in molecules and solids, *Physical Review Materials* 3 (2019) 043801. URL: <https://link.aps.org/doi/10.1103/PhysRevMaterials.3.043801>. doi:10.1103/PhysRevMaterials.3.043801.
- [16] S. Markidis, The Old and the New: Can Physics-Informed Deep-Learning Replace Traditional Linear Solvers?, *Frontiers in Big Data* 4 (2021). doi:10.3389/fdata.2021.669097.
- [17] D. Davydov, M. Kronbichler, Algorithms and Data Structures for Matrix-Free Finite Element Operators with MPI-Parallel Sparse Multi-Vectors, *ACM Transactions on Parallel Computing* 7 (2020). URL: <http://arxiv.org/abs/1907.01005>. doi:10.1145/3399736.
- [18] N. Beams, A. Abdelfattah, S. Tomov, J. Dongarra, T. Kolev, Y. Dudouit, High-Order Finite Element Method using Standard and Device-Level Batch GEMM on GPUs, in: *Proceedings of ScalA 2020: 11th Workshop on Latest Advances in Scalable Algorithms for Large-Scale Systems, Held in conjunction with SC 2020: The International Conference for High Performance Computing, Networking, Storage and Analysis, 2020*, pp. 53–60. doi:10.1109/ScalA51936.2020.00012.
- [19] D. A. Kopriva, *Implementing Spectral Methods for Partial Differential Equations*, Scientific Computation, Springer Netherlands, Dordrecht, 2009. URL: <http://link.springer.com/10.1007/978-90-481-2261-5>. doi:10.1007/978-90-481-2261-5.
- [20] A. Solomonoff, A fast algorithm for spectral differentiation, *Journal of Computational Physics* 98 (1992) 174–177. URL: <https://linkinghub.elsevier.com/retrieve/pii/002199919290182X>. doi:10.1016/0021-9991(92)90182-X.
- [21] S. Das, P. Motamarri, V. Gavini, B. Turcksin, Y. W. Li, B. Leback, Fast, Scalable and Accurate Finite-Element Based Ab Initio Calculations Using Mixed Precision Computing: 46 PFLOPS Simulation of a Metallic Dislocation System, in: *Proceedings of the International Conference for High Performance Computing, Networking, Storage and Analysis*, volume 11, ACM, New York, NY, USA, 2019, pp. 1–11. URL: <https://dl.acm.org/doi/10.1145/3295500.3357157>. doi:10.1145/3295500.3357157.
- [22] S. C. Brenner, L. R. Scott, *The Mathematical Theory of Finite Element Methods*, volume 15 of *Texts in Applied Mathematics*, Springer New York, New York, NY, 2008. URL: <http://link.springer.com/10.1007/978-0-387-75934-0>. doi:10.1007/978-0-387-75934-0.
- [23] J. Červený, V. Dobrev, T. Kolev, Nonconforming Mesh Refinement for High-Order Finite Elements, *SIAM Journal on Scientific Computing* 41 (2019) C367–C392. URL: <https://epubs.siam.org/doi/10.1137/18M1193992>. doi:10.1137/18M1193992.
- [24] P. Munch, K. Ljungkvist, M. Kronbichler, Efficient Application of Hanging-Node Constraints for Matrix-Free High-Order FEM Computations on CPU and GPU, in: *Lecture Notes in Computer Science (including subseries Lecture Notes in Artificial Intelligence and Lecture Notes in Bioinformatics)*, volume 13289 LNCS, Springer Science and Business Media Deutschland GmbH, 2022, pp. 133–152. URL: https://link.springer.com/10.1007/978-3-031-07312-0_7. doi:10.1007/978-3-031-07312-0_{_}7.
- [25] M. O. Deville, P. F. Fischer, E. H. Mund, *High-Order Methods for Incompressible Fluid Flow*, Cambridge University Press, 2002. URL: <https://www.cambridge.org/core/product/identifier/9780511546792>

type/book. doi:10.1017/CB09780511546792.

- [26] G. Fedorov, L. Huot, Intel® Math Kernel Library Improved Small Matrix Performance Using Just-in-Time (JIT) Code Generation for Matrix Multiplication (GEMM), 2019. URL: <https://www.intel.com/content/www/us/en/developer/articles/technical/onemkl-improved-small-matrix-performance-using-just-in-time-jit-code.html>.
- [27] D. Arndt, W. Bangerth, M. Feder, M. Fehling, R. Gassmöller, T. Heister, L. Heltai, M. Kronbichler, M. Maier, P. Munch, J. P. Pelteret, S. Sticko, B. Turcksin, D. Wells, The deal.II library, Version 9.4, *Journal of Numerical Mathematics* 30 (2022) 231–246. doi:10.1515/JNMA-2022-0054.
- [28] C. Burstedde, L. C. Wilcox, O. Ghattas, p4est : Scalable Algorithms for Parallel Adaptive Mesh Refinement on Forests of Octrees, *SIAM Journal on Scientific Computing* 33 (2011) 1103–1133. URL: <http://epubs.siam.org/doi/10.1137/100791634>. doi:10.1137/100791634.
- [29] T. Gruber, J. Eitzinger, G. Hager, G. Wellein, LIKWID, 2022. URL: <https://doi.org/10.5281/zenodo.7432487>. doi:10.5281/zenodo.7432487.
- [30] Y. Zhou, Y. Saad, M. L. Tiago, J. R. Chelikowsky, Self-consistent-field calculations using Chebyshev-filtered subspace iteration, *Journal of Computational Physics* 219 (2006) 172–184. doi:10.1016/J.JCP.2006.03.017.
- [31] D. P. O’Leary, The block conjugate gradient algorithm and related methods, *Linear Algebra and its Applications* 29 (1980) 293–322. URL: <https://linkinghub.elsevier.com/retrieve/pii/0024379580902475>. doi:10.1016/0024-3795(80)90247-5.